Chapter 4

Fluorescent molecules diffusing in confinement

Overview

In this chapter the nanoscale-confined diffusion of fluorescent probe molecules inside self-ordered alumina nanopores is studied for the case that the long axis of the pores coincides with the optical axis of a confocal microscope. Section 4.1 presents the experimental results. Autocorrelation and fluorescence lifetime analysis of the fluorescence signal are used as efficient tools to study macromolecules in a channel-type confinement. Section 4.2 deals with the question if water- or oil-immersion objectives are favorable for measurements in porous alumina. Monte-Carlo simulations of two-dimensional confinement (which leads to one-dimensional diffusion) and for comparison in unconfined systems (which leads to three-dimensional diffusion) are presented in section 4.4. Comparing these simulations with the experimental findings allows developing a more detailed picture of diffusion within confinement. In section 4.3 the adsorption behavior of eGFP at the pore walls is discussed as a function of the pH-value of the used buffer. First measurments of the fluorescence resonance energy transfer of doubly labeled proteins in porous alumina are presented in section 4.5.

4.1 One dimensional diffusion in porous alumina

The alignment of the long axis of the pores with the optical axis of the confocal microscope as it has been described in section 3.2 forces the probe molecules to diffuse parallel to the long axis of the laser focus, which possesses an ellipsoidal shape with short half axis $w_0 \simeq 250\,\mathrm{nm}$ and long half axis $z_0 \simeq 1000\,\mathrm{nm}$ (checked by scanning fluorescent latex-beads). The cover glass thickness correction capability of the microscope objective was used to compensate for the mismatch of refractive indices between water ($n_{\mathrm{H_2O}} = 1.33$) and the water-filled membrane treated as an effective medium with $n_{\mathrm{Alox}} = 1.57$ [48], which is possible due to the similarity of the refractive indices of glass ($n_{\mathrm{Glass}} = 1.52$) and water-filled porous alumina. This will be elaborated more in detail in section 4.2.

As long as the pore diameter is much smaller than the size of the laser focus, only movements of the molecules in the z-direction lead to intensity fluctuations. The measurements were per-

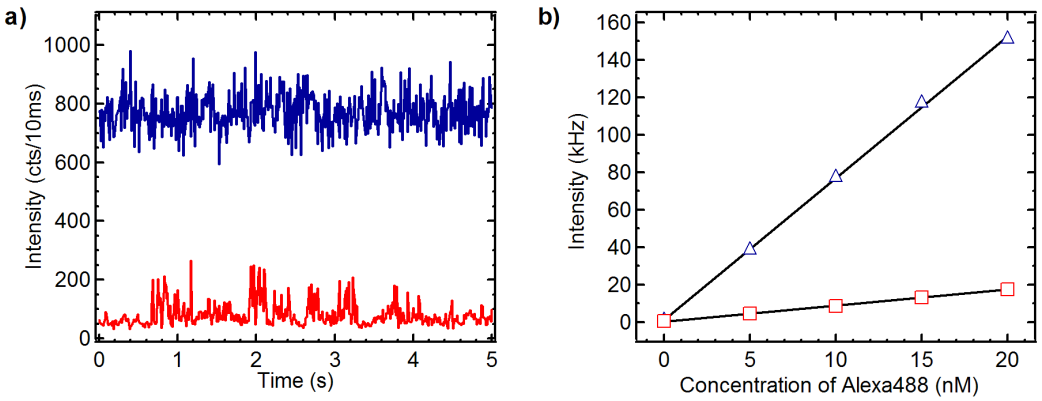

Figure 4.1: a) Transient fluorescence intensities for the dye Alexa Fluor 488 10 nM in bulk solution (top trace) and nanopore-confined solution (bottom trace) excited at 470 nm with a power of 8 μW. **b)** Average intensity for different dye concentrations in bulk solution (-△-) and inside the nanopores (-□-). The count rate increases linearly (solid line) with the concentration of the dye in the solution.

formed using the set-up described in reference [4] and using a linear actuator for positioning of the membrane with respect to the focus of the confocal microscope (see section 3.2 for details). For recording time traces at a stationary point, the focus was either placed 10 µm within the membrane or 10 µm below the membrane. This scheme allows recording of transients for one and the same stock inside the membrane and in free solution. Prior to any measurement, the membranes and the chamber were incubated over night with 107 µM bovine serum albumin in order to prevent the fluorescent molecules from unspecific adsorption. After incubation, the membranes were rinsed with deionized water.

For the first measurements, the 10 mM phosphate buffered saline (PBS) buffer (+137 mm NaCl, +2.7 mm KCl, *pH* 7.4, Sigma–Aldrich). PBS buffer was filled into the chamber and the background intensity of the buffer and the buffer-filled porous alumina membrane was recorded. Both background count rates were smaller than 1000 photons per second ($\hat{=}$1 kHz). Some microliter of a 100 nM stock solution of Alexa Fluor 488 were consecutively added to increase the concentration of the dye in the chamber. Figure 4.1 **a)** shows the transient fluorescence intensity for a 10 nM solution of Alexa Fluor 488 in buffer inside the membrane, and, for comparison, in bulk solution. The two transients clearly differ both in the average intensity, which is 77 kHz (770 photons/10 ms) in bulk solution and 9 kHz (90 photons/ 10ms) within the membrane, and their shape; the transient within the membrane shows a pronounced burst-like behavior. As shown in figure 4.1 **b)**, the detected intensity depends linearly on the dye concentration. The ratio between the slopes of the plots showing the fluorescence intensities inside the membrane and in the bulk as a function of the concentration is 1 to 9.

Similar behavior is found for eGFP, the second analyte that was investigated. Figure 4.2 **a)** shows a typical fluorescence transient for 10 nM eGFP in bulk solution and within the porous alumina membrane. In addition to the pronounced fluorescence bursts like those observed for Alexa Fluor 488 within the membrane, a slow decrease of the background signal was found. If the laser is switched off and on again, the background signal recovers and decays again. Again, as shown in figure 4.2 **b)**, the detected intensity depends linearly on the concentration of eGFP, but the ratio of the slopes in this case is only 1 to 4.

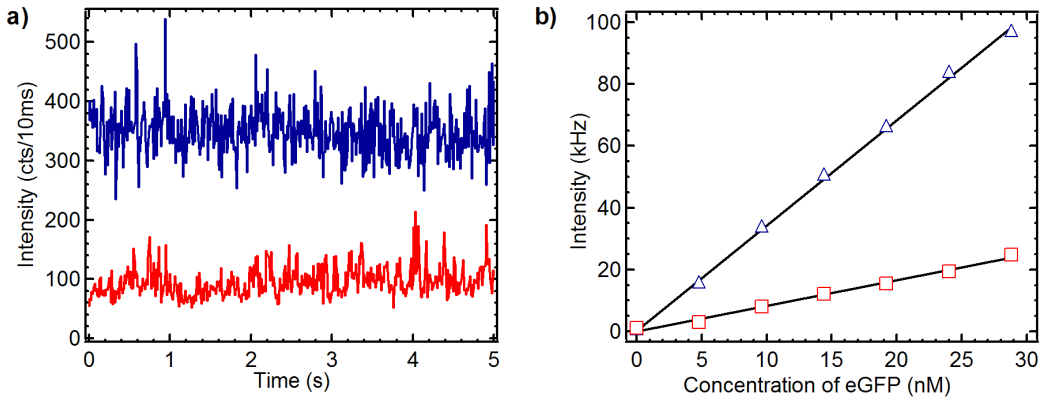

Figure 4.2: **a)** Transient fluorescence intensities for eGFP 10 nM in bulk solution (top trace) and nanopore-confined solution (bottom trace) excited at 470 nm with a power of 8 μW. **b)** Average intensity for different protein concentrations in bulk solution (-△-) and inside the nanopores (-□-). The count rate increases linearly (solid line) with the concentration of the dye in the solution.

The intensity drop inside the membrane could be caused by either one or a combination of the following effects: a lower average number of molecules in the detection volume, a reduced excitation intensity, a quenched emissive rate of the molecules or a reduced detection efficiency. The first effect concerns just the apparent concentration whereas the latter three would change the molecular brightness, i.e. the apparent fluorescence intensity per molecule. The actual reason will be elaborated in detail in the following.

The quantity related to the apparent concentration of molecules within the detection volume is the amplitude $G(\tau = 0) = 1 + 1/N$ of the auto-correlation functions (ACFs), which are shown in figure 4.3 **a)**. $G(0)$ is decreasing with increasing dye concentration, and is considerably lower in bulk solution than within the membrane. The obtained average number of dye molecules in the detection volume N is plotted versus the dye concentration in figure 4.3 **b)**. A linear dependence is obtained, where the slope for the bulk data is about 3 times the slope within the membrane. Therefore, the apparent particle number in the membrane is lowered by a factor of three, which is in reasonable agreement with the reduced detection volume inside the membrane assuming a porosity of 20-25%. Note that the intercept of the lines is essentially zero, which indicates the reliability of the method.

Figure 4.4 **a)** shows the ACF for 10 nM eGFP in bulk solution and within the membrane. Both functions have the same amplitude indicating an almost equal apparent number of molecules within the detection focus. As shown in figure 4.4 **b)**, this is the case for each concentration of eGFP.

It is known from literature that uncorrelated background, which is here assigned to immobilized eGFP molecules for the measurement inside the membrane, has a huge impact on the apparent mean number of molecules [54]. The assignment of the background signal to immobilized molecules is supported by the finding that the average count rate of eGFP is not reduced as much as for the Alexa dye. The integral intensity from membranes soaked with eGFP solution is thus the sum of diffusing molecules (as measured by FCS) and of immobilized molecules. Assuming the same reduction of the effective confocal volume within the membrane as for the Alexa dye, we can estimate the number of molecules causing the constant background.

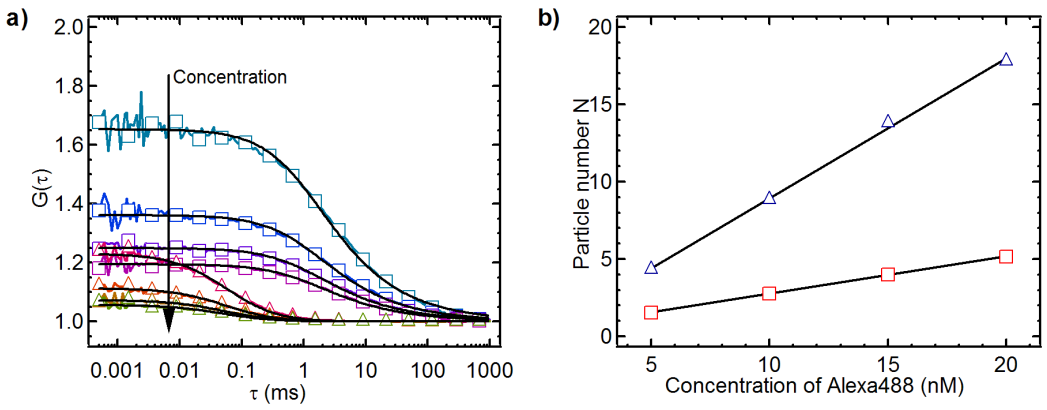

Figure 4.3: a) Intensity auto-correlation functions for transients of different concentrations of Alexa Flour 488 in bulk solution (△) and in the nanopores (□). The solid lines are fits according to equations 2.21 and 2.19 assuming three-dimensional and one-dimensional diffusion, respectively. **b)** Mean particle numbers N in the confocal volume as a function of dye concentration in bulk solution (-△-) and inside the nanopores (-□-). Straight lines represent linear fits.

The ratio between the fluorescence intensity reduction factors $r = I_{\text{bulk}}/I_{\text{Alox}}$ for the Alexa dye ($r_{\text{Alexa}} \approx 9$) and for eGFP ($r_{\text{eGFP}} \approx 4$) is $r_{\text{Alexa}}/r_{\text{eGFP}} \approx 2$. Therefore, it can be concluded that the total concentration of eGFP molecules in the confocal volume is two times the concentration expected from the effective concentration. In conclusion, the number of immobile molecules N_{immob} equals the number of mobile molecules N_{mob}. This conclusion can be further evidenced looking at the results from the correlation analysis. The apparent number of molecules N_{app} as measured by FCS in the presence molecules contributing uncorrelated background is given by [54]

$$N_{\text{app}} = \frac{(N_{\text{mob}} + N_{\text{immob}})^2}{N_{\text{mob}}}. \tag{4.1}$$

With $N_{\text{mob}} \approx N_{\text{immob}}$ one gets $N_{\text{app}} \approx 4N_{\text{mob}}$. This is in clear accordance with the experimental results: The apparent number of molecules in the focus for eGFP is by a factor of about 4 larger

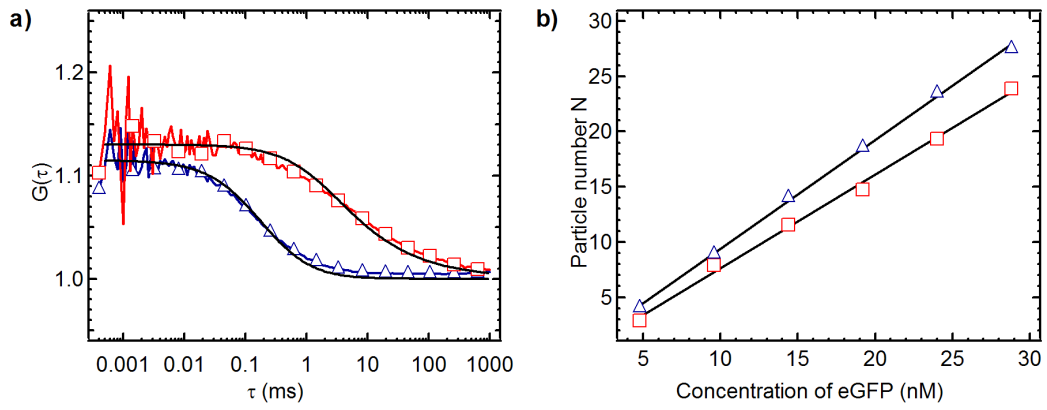

Figure 4.4: a) Intensity auto-correlation functions for transients of 10 nM eGFP in bulk solution (-△-) and in the nanopores (-□-). The solid lines are fits according to equations 2.21 and 2.19 assuming three-dimensional and one-dimensional diffusion, respectively. **b)** Apparent mean particle numbers N in the confocal volume as a function of eGFP concentration in bulk solution (-△-) and inside the nanopores (-□-). Straight lines represent linear fits.

than the value expected from the porosity of the membrane. On the other hand, assuming a tenth of a monolayer of BSA at the pore walls [57], one can estimate that some tens of thousands BSA molecules are located within the detection volume based on geometry considerations. The fraction of immobilized eGFP molecules related to the total amount of adsorbed protein is thus extremely small. Here, it is additionally assumed that the emitted fluorescence intensity is the same for diffusing and immobilized molecules, respectively, i.e., no fluorescence quenching is taken into account.

An important parameter in FCS is the molecular brightness, which is defined as the average intensity divided by the mean particle number N. The molecular brightness is influenced by changes in the excitation intensity and the detection efficiency, respectively, and by quenching of fluorescence. Figure 4.5 shows the average intensity as a function of the apparent particle number N for **a)** Alexa Fluor 488 and **b)** eGFP. Straight lines represent linear fits yielding the molecular brightness parameter; for Alexa Fluor 488 in bulk solution $B^{\text{Alexa}}_{\text{bulk}} = 8.3\,\text{kHz/molecule}$ and in the membrane $B^{\text{Alexa}}_{\text{Alox}} = 3.6\,\text{kHz/molecule}$. For eGFP, the corresponding numbers are $B^{\text{eGFP}}_{\text{bulk}} = 3.5\,\text{kHz/molecule}$ and $B^{\text{eGFP}}_{\text{Alox}} = 1.0\,\text{kHz/molecule}$. For Alexa Fluor 488, the molecular brightness is reduced by a factor of $R_{\text{Alexa}} = B^{\text{Alexa}}_{\text{bulk}}/B^{\text{Alexa}}_{\text{Alox}} = 2.3$. This is caused by the fact that the detection angle is lowered within the membrane. A water-immersion objective ($n_{\text{H}_2\text{O}} = 1.33$) featuring a numerical aperture of $N_A = 1.2$ has a half detection angle of $\alpha_{H_2O} = 64^\circ$ based on the equation

$$N_A = n \sin \alpha. \tag{4.2}$$

With the effective refractive index in the membrane of $n_{\text{Alox}} = 1.57$ the half angle amounts to $\alpha_{\text{Alox}} = 50^\circ$, which results in a decrease of the steradian of which photons can be detected. The ratio of these accessible solid angles for $\alpha_{\text{H}_2\text{O}}$ and α_{Alox} can be calculated according to the equation for the steradian

$$\Omega = 2\pi\,(1 - \cos\alpha)\,. \tag{4.3}$$

The reduction of the detectable fluorescence within the alumina membrane can be calculated to be a factor of $R_\Omega = \Omega_{64\circ}/\Omega_{50^\circ} = 1.7$, which is in reasonable agreement with the measured value for the Alexa dye ($R_{\text{Alexa}} = 2.3$). In the case of eGFP, the brightness was calculated with the apparent particle number $N_{\text{app}} = 2 * (N_{\text{mob}} + N_{\text{immob}})$. Taking only the real particle number ($N_{\text{real}} = N_{\text{mob}} + N_{\text{immob}}$) into account leads to $R_{eGFP} = 1.8$, which is in perfect agreement with the expectation of $R_\Omega = 1.7$.

In order to elucidate quenching effects due to pore-wall interactions, the fluorescence decay time of the dyes in the membrane was compared with the decay time in bulk solution. Contacts with the pore walls may lead to fluorescence quenching, which can be experimentally identified by a shortening of the fluorescence decay time. Besides quenching processes, the refractive index of the medium surrounding the emitter can modify the fluorescence lifetime τ_f via the radiative lifetime $\tau_0 = 1/k_{\text{rad}}$, which is inversely proportional to the square of the refractive index reading [94]

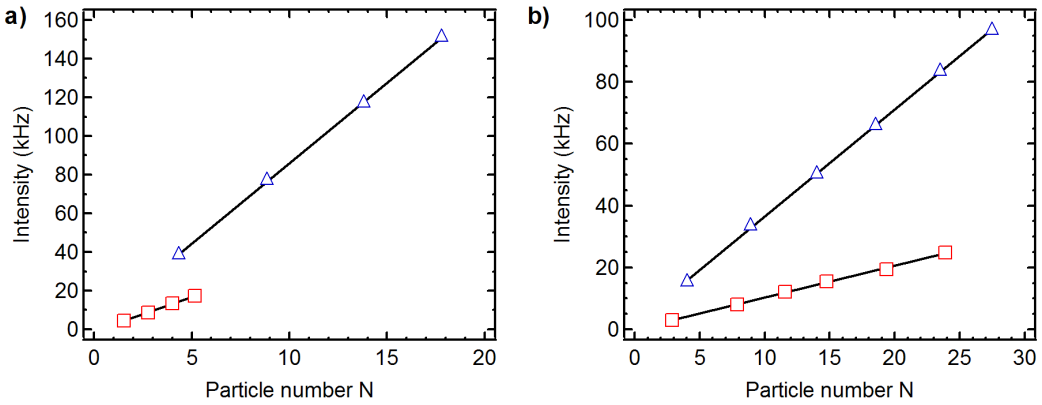

Figure 4.5: Average fluorescence intensity versus the particle number N in bulk solution (-△-) and in the nanoporous membrane (-□-) for different concentrations of **a)** Alexa Fluor 488 and **b)** eGFP. The solid lines represent linear fits, where the slope represents the moleculear brightness.

$$\frac{n_{\mathrm{M}}^2}{n_{\mathrm{H_2O}}^2} = \frac{\tau_{\mathrm{f,H_2O}}}{\tau_{\mathrm{f,M}}}. \tag{4.4}$$

For Alexa Fluor 488 the fluorescence decays follow a single-exponential law appearing as straight lines in the semilogarithmic plot in figure 4.6 **a)**. A decrease of the fluorescence lifetime from $\tau_{\mathrm{f,H_2O}} = 4.1\,\mathrm{ns}$ in bulk solution to $\tau_{\mathrm{f,M}} = 3.0\,\mathrm{ns}$ within the membrane was found for all dye concentrations. For Alexa Fluor 488 with its fluorescence quantum yield close to unity in solution, the fluoresence decay is nearly exclusively governed by the radiative rate k_{10} as discussed in section 2.1. With the refractive index of $n = 1.57$ for the water-filled membrane one can expect a fluorescence lifetime of $\tau_{\mathrm{f,M}} = 2.9\,\mathrm{ns}$ within the membrane, which matches the experimental result almost perfectly.

For eGFP, as it is shown in figure 4.6 **b)**, a mono-exponential fit model was applied, which reflects the shortening of the fluorescence decay due to refractive-index changes following Suhling's approach [96]. A fluorescence lifetime of $\tau_{\mathrm{f,H_2O}} = 2.6\,\mathrm{ns}$ in bulk solution and $\tau_{\mathrm{f,M}} = 2.2\,\mathrm{ns}$ in the membrane was obtained. The quantum yield of fluorescence $\Phi_{\mathrm{f}} = k_{\mathrm{rad}}/(k_{\mathrm{rad}} + k_{\mathrm{nrad}}) = k_{\mathrm{rad}} \cdot \tau_{\mathrm{f}}$ for eGFP is $\Phi_{\mathrm{f}} = 0.6$ [75]. Combining the Strickler-Berg formula with the definition of the fluorescence quantum yield,

$$\tau_{\mathrm{f,M}} = \left(\frac{\Phi_{\mathrm{f}}}{\tau_{\mathrm{f,H_2O}}} + \frac{1-\Phi_{\mathrm{f}}}{\tau_{\mathrm{f,H_2O}}} \frac{n_{\mathrm{M}}^2}{n_{\mathrm{H_2O}}^2} \right)^{-1}, \tag{4.5}$$

a fluorescence decay time in the membrane of $\tau_{\mathrm{f,M}} = 2.2\,\mathrm{ns}$ can be estimated, which is again in perfect agreement with the experimental result, indicative of the absence of quenching processes. At first, this finding is surprising because there are immobilized molecules in the membrane that might be prone to quenching. The chromophore of eGFP, however, is known to be shielded by the protein structure from the environment, thus preventing collisional quenching by pore-wall contacts. Let us now focus on the dwell time of the molecules in the focal volume, which is related to the decay of the ACFs in figure 4.3 **a)**. The solid lines represent fits to the experimental ACFs with the one-dimensional model using equation 2.19 for the signal measured inside the membrane and with the three-dimensional model using equation 2.21 in bulk

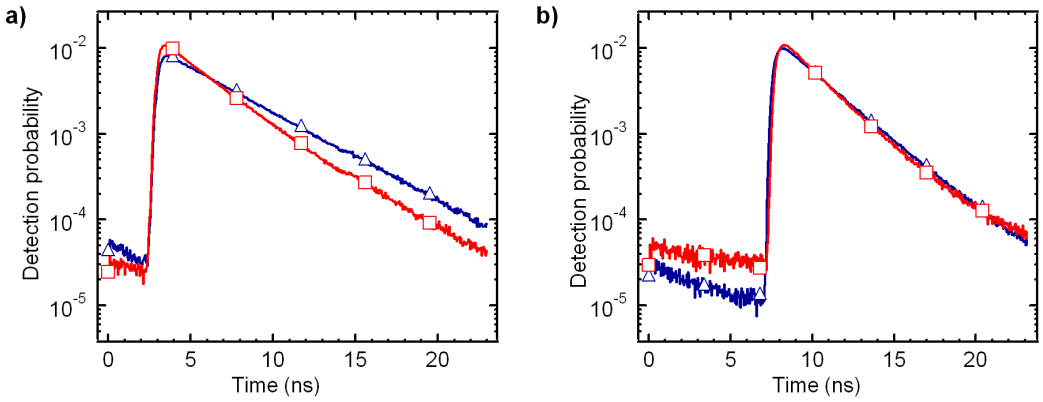

Figure 4.6: **a)** Fluorescence decay for 10 nM Alexa Fluor 488 in bulk solution (-△-) and in the nanoporous membrane (-□-). **b)** Fluorescence decay for 10 nM eGFP in bulk solution (-△-) and in the nanoporous membrane (-□-).

solution, respectively. All ACFs were corrected for afterpulsing by application of a temporal filter as described in section 2.5. The excellent agreement of the fitted curves and the experimental auto-correlation functions for the transients taken inside the nanopores is evidence of apparent one-dimensional diffusion. No long-time component is apparent in the ACFs, demonstrating the absence of sticking effects. Defining the diffusion time for the unconfined diffusion as $\tau_D^{3D} = \omega_0^2/4D$ and for one-dimensional diffusion as $\tau_D^{1D} = z_0^2/4D$, the ratio between the diffusion time in the one-dimensional case along z and in the three-dimensional case is just the square of the structural parameter s, which is defined as $s = z_0/w_0$ and amounts to $s \simeq 4$ in the microscope which was used. Therefore, one can expect a $s^2 = 16$ times longer diffusion time τ_D inside the membrane as compared to free bulk diffusion. The ratio between the visually easier to access ACF decay half times $\tau_{1/2}$, however, is even larger due to the different exponents of the diffusion terms. The fits of the model functions to the experimental ACFs yield diffusion times $\tau_D^{3D} = 54 \pm 3\,\mu s$ in bulk solution and $\tau_D^{1D} = 1003 \pm 30\,\mu s$ in the membrane with negligible variations between the different concentrations. The diffusion time τ_D^{1D} is thus 19 times longer than in free solution. This is in reasonable agreement with the applied model and indicates moreover that the diffusion time of Alexa Fluor 488 molecules is not affected by interactions between the analyte and the pore walls. The same holds for eGFP, where a 14 times increased diffusion time was found in the membrane as compared to bulk solution, which is indicating that the mobile fraction of the probe molecules is not slowed down by interactions with the pore wall. One can only speculate that the deviations of the experimental ACFs from the model functions in solution as well as under confinement for eGFP are related to the inherent photophysics of the eGFP chromophore [39].

4.2 Objectives: water-immersion versus oil-immersion

Water-immersion objective

All results in the previous section were obtained using a water-immersion objective with a correction ability for the cover glass thickness. Here, this correction ability is used to compensate

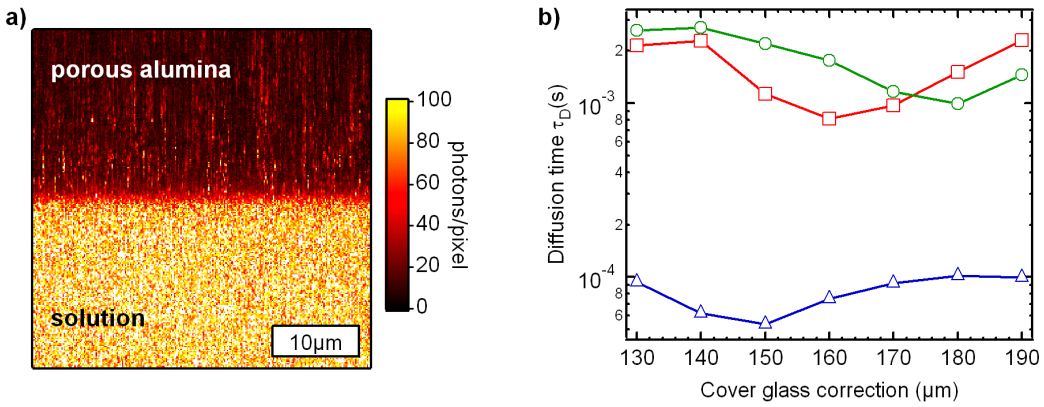

Figure 4.7: a) Fluorescence scanning image of Alexa Fluor 488 diffusing in solution and within the porous alumina membrane. The stripe-like features within the membrane correspond to the diffusion of the molecules along the pores (which coincides with the z- direction). **b)** Influence of the cover glass correction of the water-immersion objective on the diffusion time of 6.5 nM Alexa Fluor 488 diffusing in bulk solution 10 µm below the solution/membrane interface (-△-), 10 µm within the membrane (-□-), and 20 µm within the membrane (-◯-) . Note the logarithmic scale of the diffusion time.

the distortions of the focus in the alumina membrane, which are caused by a mismatch of the refractive indices of water $n_{H_2O} = 1.33$ and the water filled membrane $n_{Alox} = 1.57$. To elaborate this correction more in detail, an experiment was performed, where the diffusion time and the brightness was measured as a function of the specified objective cover glass correction. In contrast to the set-up used for the previous measurments as described in reference [4], the set-up described in section 3.2 has the ability to scan along the membrane. The excitation intensity was 10 µW at 470 nm. A polarizing beam splitter was used to split the fluorescent light into two detectors. This configuration allows for cross-correlating the signals without any need of applying an afterpulsing filter. Alexa Flour 488 was used as the fluorescent probe and the concentration of the dye was adjusted to 6.5 nM in PBS buffer. Due to the fact that the membrane was attached to a linear actuator whose position cannot be controlled via the x- and y-positioning stage, the image in figure 4.7 **a)** shows only a set of line scans along the z-direction, without any real change in the x- or y-direction. Nevertheless, several points should be noted: 1) as expected, the mean intensity per pixel in solution is larger than within the porous alumina, 2) there is no adsorption of Alexa Fluor 488 at the solution/membrane interface, which would result in a massively increased intensity per pixel at the interface and 3) within the porous alumina, strip-like intensity features are visible, which correspond to fluorescent molecules diffusing along the fast scanning axis of the focus.

Figure 4.7 **b)** shows the mean diffusion times calculated from the cross-correlation functions for three positions of the focus as a function of the cover glass correction. The focus was either placed 10 µm below the membrane, or 10 µm and 20 µm, respectively, within the membrane. The standard thickness of a cover glass slide is 150 µm, using this value for correction provides the smallest measurable diffusion time, which gives $\tau_D = 62$ µs in free solution. If the cover glass correction is changed, the diffusion time increases up to a factor of two. If the focus is placed 10 µm within the membrane, the diffusion time is minimized for a correction factor of 160 µm. Similar to the measurements in the previous chapters, the diffusion time within the membrane equals $\tau_D \simeq 1$ ms. Again, if the cover glass correction is changed, the measured

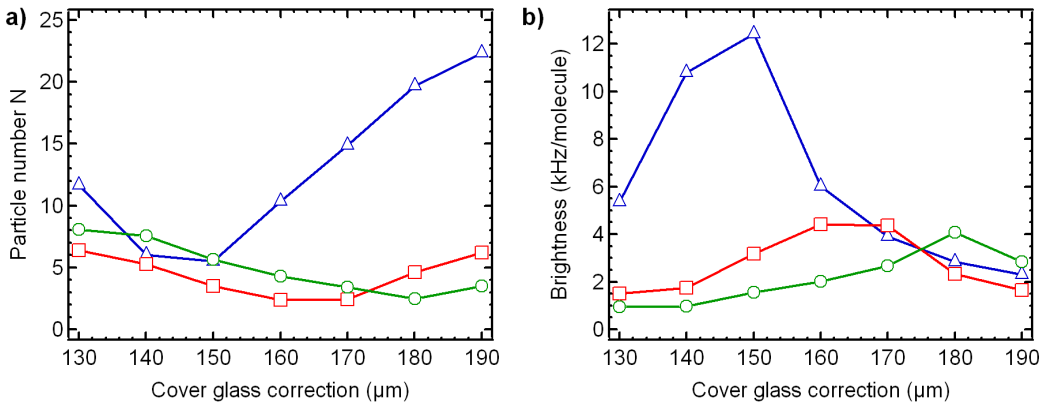

Figure 4.8: Influence of the cover glass correction of the water-immersion objective on **a)** the mean particle number N and **b)** the brightness B of 6.5 nM Alexa Fluor 488 diffusing in bulk solution 10 µm below the solution/membrane interface (-△-), 10 µm within the membrane (-□-), and 20 µm within the membrane (-◯-). The minimized particle number and the maximized brightness for each line indicates the smallest obtainable focus as a function of the cover glass correction.

diffusion time increases. However, in contrast to the measurement in free solution, where the three-dimensional correlation fitting function is due to $D_{3D} = w_0^2/4\tau_D$ mainly sensitive to the elongation of the focus in the x- and y-direction, the one-dimensional correlation fitting function is only sensitive to the elongation of the focus in the z-direction according to $D_{1D} = z_0^2/4\tau_D$. If the focus is placed 20 µm within the membrane, the diffusion time is minimized using a cover glass correction value of 180 µm. This value is slightly higher than the value of 170 µm obtained by just adding the coverglass thickness and the depth within the membrane, which can be explained by the fact that the refractive index of water-filled porous alumina is slightly larger than that of the cover glass ($n_{glass} = 1.52$).

As mentioned above, the diffusion time is not only sensitive to the dimensions of the excitation/detection focus. Additional useful parameters are the mean particle number N and the molecular brightness B, which is defined as $B = \text{countrate}/N$. Figure 4.8 **a+b)** shows the mean particle number and the molecular brightness as a function of the cover glass correction factor for the three positions of the focus. Mainly, the lines are following the behavior of the diffusion time: if the diffusion time τ_D is minimized by the cover class correction, the particle number N is minimized, too, and thereby the brightness B is maximized. Let us take a closer look at the measurements in solution. If the value of the cover glass correction is between 170 µm and 190 µm, the diffusion time is more or less constant. In contrast, the particle number increases dramatically and therefore the brightness decreases. This finding can be explained by an expansion of the focus in z-direction and will be elaborated more in detail via Monte-Carlo simulations in section 4.4. Within the membrane, this effect (here on the expansion of the focus in the x- and y-plane) is too small to be clearly visible. In conclusion, the cover glass correction of the water-immersion objective provides a practicable tool to adjust the focus for measurements within porous alumina. Nevertheless, the mismatch of the refractive indices of water and water-filled porous alumina leads to an decreased molecular brightness within the membrane due to the reduction of the detection angle.

In contrast to the previous experiments in this section, the following experiment uses the experimental configuration shown in figure 3.2 **b)**, which allows for real scanning in the x- and

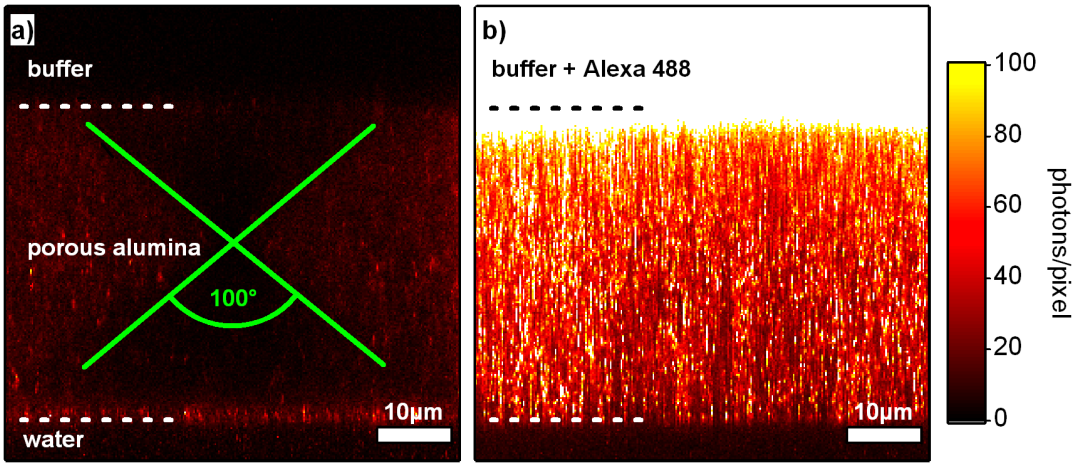

Figure 4.9: Color coded scanning images of a citrate buffer filled porous alumina membrane. The membrane was attached via pure water to the cover glass using an water-immersion objective for excitation and detection. The size of the image is 60 µm x 60 µm scanned with a resolution of 256 x 256 pixels and a time resolution of 1 ms/pixel. The dashed lines represent the buffer/membrane interface. **a)** Background intensity of the water filled membrane after bleaching for several minutes at the position of the crossed lines. The detection angle $2 \cdot \alpha$ is about 100°. **b)** After adding some micro liter of 130 nM Alexa Fluor 488 to reach a concentration of 6.5 nM in the solution, no adsorbing of the fluorescent protein at the water/membrane interface takes place. Moreover, this image was taken after recording a transient time trace within the membrane. No bleaching of molecules is visible.

z-plane. The excitation was performed at 40 µW using circulary polarizied laser light at a wavelength of 488 nm. A polarizing beamsplitter was used to split the fluorescent light into orthogonally polarized components. Figure 4.9 **a)** shows the background image of the buffer-filled membrane after taking a transient time trace at the crossing of the green lines. Laser irradiation leads to the bleaching of fluorescent contaminants in the alumina membrane. The bleached region can be used to estimate the detection angle according to $2 \cdot \alpha_{Alox} = 100°$ within the membrane, which is in perfect agreement with the theoretical calculated value in section 4.1. After addition of Alexa Fluor 488, the focus was placed at the center of the membrane to record a transient time trace. Subsequent recording of figure 4.9 **b)** shows the penentration of the membrane and the absence of a bleached region indicating a good mobility of the probe.
The main idea behind this measurement is shown in figure 4.10. Whereas in the previous part auto-correlation functions were calculated for different depths within the membrane using fixed correction settings of the water-immersion objective, here the correction was changed as a function of the depth within the membrane. Assuming a cover slide thickness of 150 µm, the collar ring of the objective was set to 150 µm. For each increase of the depth of the focus within the membrane (counted from the water/membrane interface), the collar ring was adjusted to the value of the cover slide plus the depth within the membrane. Indeed, as shown in figure 4.10 **a)**, the correction works sufficiently well. The diffusion time is around 1 ms in almost any depth. Only at higher depths and thereby close to the membrane/buffer interface deviations are clearly visible. These deviations can be attributed either to the non-ideal corrrection because of the higher refractive of the membrane compared to the cover slide or the beginning influence of the freely diffusing molecules above the membrane. Moreover, as shown in figure 4.10 **b)**,

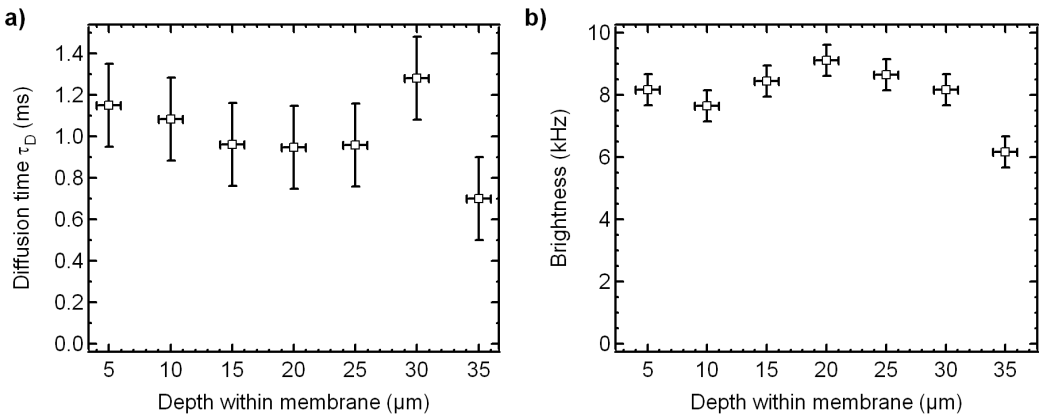

Figure 4.10: Alexa Fluor 488 diffusing within porous alumina using an water-immersion objective. **a)** diffusion time τ_D and **b)** molecular brightness as a function of the depth within the membrane (closed bottom), whereas the first water/membrane interface was set to zero. The correction ring of the water-immersion objective was set to 150 µm for the cover glass thickness plus the respective depth within the membrane.

the molecular brightness remains constant with increasing depth of detection in the membrane, demonstrating that the correction capability of the water-immersion objective can be used efficiently to compensate the spherical aberrations even in relatively large depths within a alumina membrane.

Oil-immersion objective

In order to overcome the problems caused by the decreased detection angle, I will now concentrate on the use of an oil-immersion objective instead of a water-immersion objective. The oil-immersion objective is corrected for measurements in objects with a refractive index of $n_{\text{Oil}} = 1.52$, which is close to the refractive index of the porous alumina membrane with $n_{\text{Alox}} = 1.57$. The oil-immersion objective has a numerical aperture of $NA = 1.4$, resulting in a detection angle of $2 \cdot \alpha = 2 \cdot 67^\circ = 134^\circ$.

In contrast to the experiments discussed above, where no adsorption of the fluorescent molecules at the solution/membrane interface occured, the following experiment shows a strong adsorption, thereby giving for example direct access to the detection angle. Figure 4.11 shows scanning images of a water-filled porous alumina membrane. This membrane was attached with immersion oil to the cover glass. The scanning area was 80 µm x 80 µm scanned with a resolution of 256 x 256 pixels and a time resolution of 1 ms per pixel. The laser power was adjusted to 60 µW at a wavelength of 488 nm. The background intensity of the system is shown in figure 4.11 **a)**. The intrinsic luminescence of the porous alumina membrane slightly exceeds the mean intensity in water. After adding some microliter of Barstar 488/594 solution in order to reach a concentration of 9 nM in the solution, figure 4.11 **b)** was recorded. The scanning along the pores took place from the right side to the left. If the scanning parameters are taken into account, the whole image is recorded in approximately one minute. This allows for imaging both the evolution of the adsorption of the molecules at the membrane/solution interface as indicated by the black arrow and the penetration of the membrane by the labeled protein as indicated by the green arrows. The count rate at the interface massively exceeds the range cov-

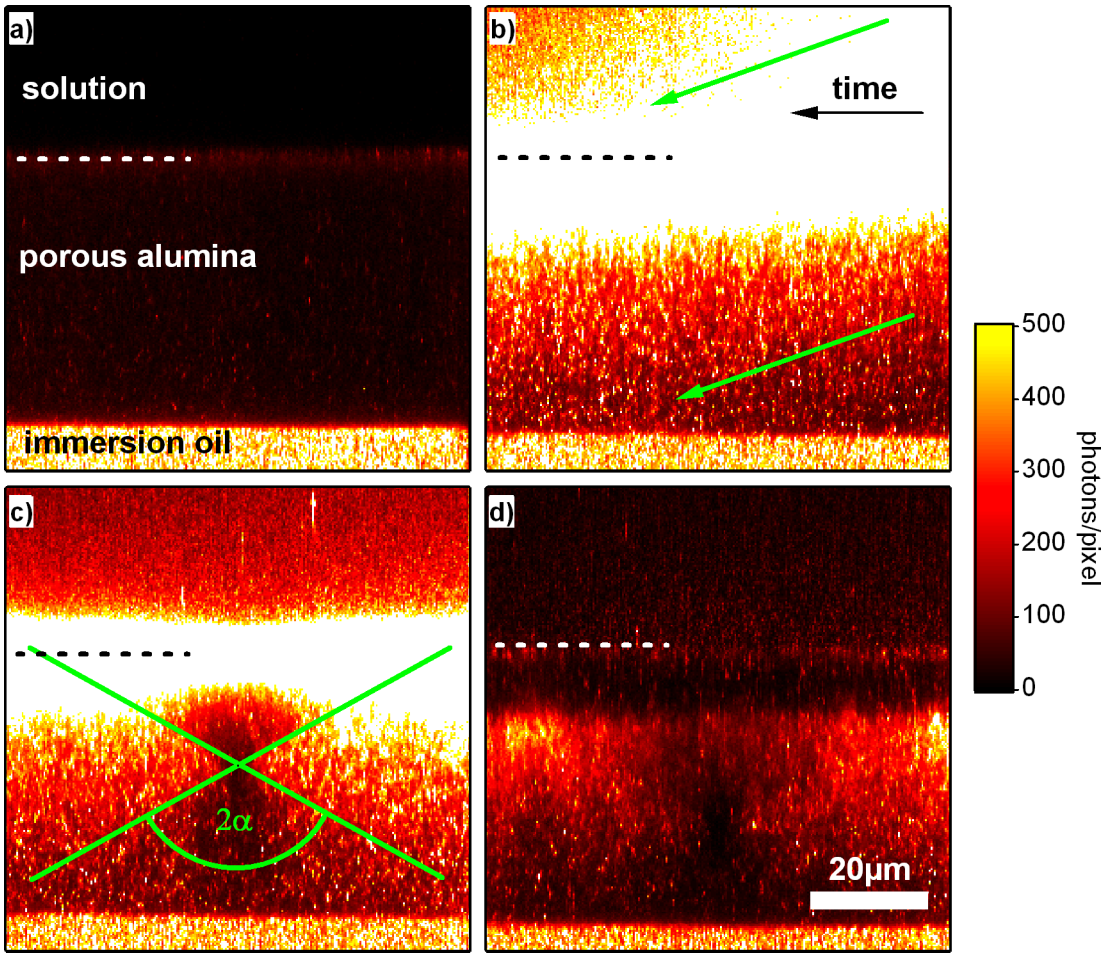

Figure 4.11: Color-coded scanning images of a water-filled porous alumina membrane. The membrane was attached via immersion oil to the cover glass using an oil-immersion objective for excitation and detection. The size of the image is 80 µm x 80 µm scanned with a resolution of 256 x 256 pixels. The dashed lines represent the water/membrane interface. **a)** Background intensity of the water filled membrane. **b)** After adding a few microliters of Barstar 488/594 solution to reach a concentration of 9 nM in the solution, strong adsorption of the fluorescent protein takes place at the water/membrane interface. Only a small fraction of molecules penetrate the membrane. The black arrow indicates the consecutive scanning time. **c)** Image taken after recording a longer time trace in the center of the crossed lines. The angle between the crossed lines is $2 \cdot \alpha = 123°$. **d)** Image taking several minutes after adding 5 µl of 1M KOH to increase the *pH*-value from 7 to about 11.

ered by the color scale: a mean intensity of more than 5000 photons per pixel was measured directly at the interface. Figure 4.11 **c)** was recorded after taking a transient time trace for several minutes, where the focus was stationary placed at the center of the crossed lines. Strong bleaching occurs around the beforehand fixed focus position. The bleached region indicates a large fraction of immobilized molecules within the pores. Generally speaking, recording a transient time trace at a fixed position creates an image of the bleached region as a function of the excitation intensity distribution. This image can be used to estimate the detection angle of the oil-immersion objective inside the porous alumina membrane. The detection angle (between the crossing lines in figure 4.11 **c)**) was roughly estimated according to $2 \cdot \alpha \simeq 123°$, which is in good agreement with the theoretical value of $2 \cdot \alpha_t = 126°$ within a medium with a refractive index of $n = 1.57$. Note that the oil-immersion objective has a detection angle of $2 \cdot \alpha = 134°$ in a medium with a refractive index of $n = 1.52$. Still, the detection angle of $2 \cdot \alpha \simeq 123°$ is

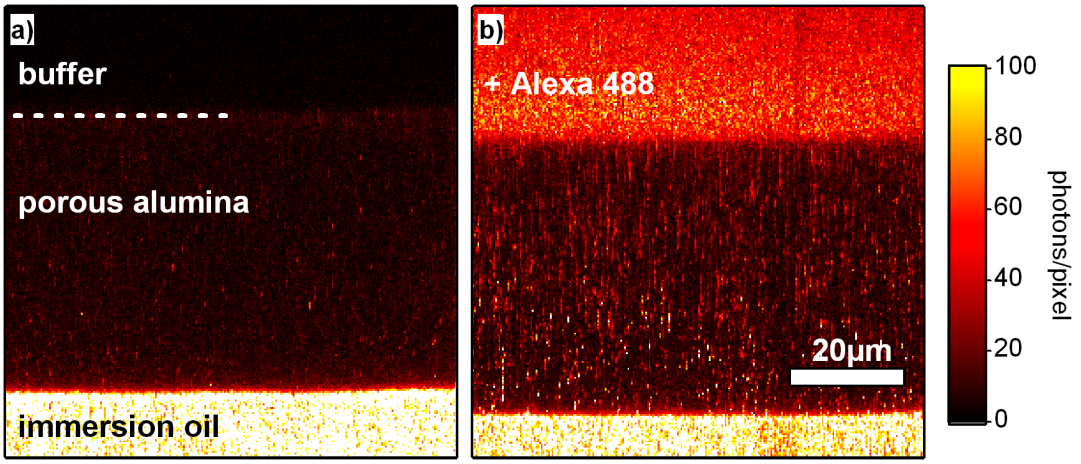

Figure 4.12: Color-coded scanning images of a citrate buffer filled porous alumina membrane. The membrane was attached via immersion oil to the cover glass using an oil-immersion objective for excitation and detection. The size of the image is 80 µm x 80 µm scanned with a resolution of 256 x 256 pixels. The dashed lines represent the buffer/membrane interface. **a)** Background intensity of the water filled membrane. **b)** After adding some micro liter of 130 nM Alexa Fluor 488 to reach a concentration of 6.5 nM in the solution, no adsorbtion of the fluorescent protein at the water/membrane interface takes place. Moreover, this image was taken after recording a transient time trace within the membrane. No bleaching of molecules is visible.

a significant improvement compared to the detection angle of $2 \cdot \alpha \simeq 100^\circ$ within porous alumina using a water-immersion objective. The next image in figure 4.11 **d)** is recorded several minutes after adding 5 µl of 1 M KOH. Note that in this experiment deionized water was used instead of a buffer, therefore the *pH*-value increases instantaneously. This might lead to several (partly overlapping) effects, namely a degeneration of the alumina membrane (and thereby consequently the release of immobilized molecules), quenching of the fluorophores due to the release of oxygen and a change in the electrostatical behavior of the pore walls.

In conclusion, this example shows that the imaging of fluorescence along the porous membrane can provide useful information even if the recording of transient time traces within the membrane does not show any meaningful auto-correlation function.

The experiment discussed in the following deals again with the diffusion of Alexa Fluor 488 within porous alumina. Figure 4.12 shows a membrane attached with immersion oil to a cover glass. Note that the pores are closed at the bottom of the membrane. The immersion oil cannot penetrate the membrane. The laser power was adjusted to 25 µW at an excitation wavelength of 470 nm. The repetition rate of the laser was set to 40 MHz. The size of the image is 80 µm x 80 µm scanned with a resolution of 256 x 256 pixels at a scanning speed of 1 ms/pixel. A polarizing beamsplitter was used to separate the detected fluorescence into two detectors. Again, the background luminescence of the membrane as shown in figure 4.12 **a)** is almost negligible. After adding Alexa Fluor 488 to the citrate buffer solution (*pH* 8), the dye penetrates the membrane instantaneously without adsorbing at the solution/membrane interface. Figure 4.12 **b)** is taken after recording a transient time trace within the membrane showing no bleaching as expected due to the lack of immobilized molecules.

The transient time traces were recorded as a function of 1) the focus position at the z-axes

within either the membrane or the solution and 2) as a function of the excitation polarization, which allows for accurate anisotropy measurements (not shown here). The oil/membrane interface corresponds to the focus position of 0 µm, whereas at a position of 45 µm the membrane/solution interface is located. Due to small shifts of the membrane in the z-direction during the measurements, the results from the different excitation polarizations at a position of 45 µm can not be compared with each other; for an excitation polarization of 0° the focus was predominantly located in solution, for an excitation polarization of 90° the focus was predominantly within the membrane.

The transient time traces were used to calculate the cross-correlation functions (not shown). Fitting these functions allows calculating the parameters shown in figure 4.13. Figure 4.13 **a)** shows the diffusion time τ_D as a function of the focus position. Interestingly, the expected diffusion time of around 1 ms (as determined by using a water-immersion objective in sections 4.1) within the membrane can only be found at a depth of about 35 µm. If the position of the focus is changed to smaller values, the diffusion time decreases to $\tau_D \simeq 0.35$ ms. As it is obvious from the MC-simulations in section 4.4, this finding can not be explained by a change in the auto-correlation function properties caused by the closed side of the pores. Moreover, a change in the diffusion coefficient would compromise previous results as discussed in section 4.1. Let us estimate the size of the focus, by taking the calculated diffusion time and the diffusion coefficient of Alexa Fluor 488 $D = 2.8 \cdot 10^{-6}\mathrm{cm}^2/\mathrm{s}$. According to $z_0 = \sqrt{4D\tau_D}$ the long half axis equals $z_0 \simeq 630$ nm. This shrinking of the excitation/detection focus is supported by figure 4.13 **b+c)**. Near the proximity of the side of the membrane with the closed pore bottoms, firstly, the mean particle number within the focus (which is in fact a function of the size of the focus) reaches a local minimum, whereas, secondly, the brightness reaches its maximum within the membrane. As shown in figure 4.13 **d)**, both findings occur with a constant count rate within the membrane. This indicates that in contrast to the mean number of fluorescent molecules within the focus, the overall concentration of molecules within the pore remains constant.

Moreover, the dimension of the focus was determined for an oil-immersion objective in reference [46]. The long axes equals $z_{0,oil} \simeq 610$ nm, which is in reasonable agreement with the calculated length of $z_0 \simeq 630$ nm by using $\tau_D \simeq 0.35$ ms. The increase of the diffusion time towards larger distances to the oil/alumina interface can again be attributed to the mismatch of the effective refractive index of water-filled porous alumina ($n_{alox} = 1.57$) to the refractive index to that the oil-immersion obejctive is corrected for ($n_{oil} = 1.52$). Due to this mismatch, spherical aberrations occur, which enlarge the dimensions of the focus in z-direction reaching approximately $z_0 = 1$ µm at a distance of 35 µm from the oil/alumina interface. Nevertheless, it has to be mentioned that according to equation 2.33 the particle number and the brightness within the membrane are strongly influenced by the background luminescence. In addition, measurements in solution ($n_{H_2O} = 1.33$) are neither corrected for the distortion of the focus which occurs after travelling through the whole membrane nor for measuring of solution with an oil-immersion objective. Therefore, the calculated values in the aqeous phase should be taken with care.

In conclusion, the oil-immersion objective has the great advantage that especially close to the oil/alumina interface, the focus is only slightly distorted and the detection angle is close to the

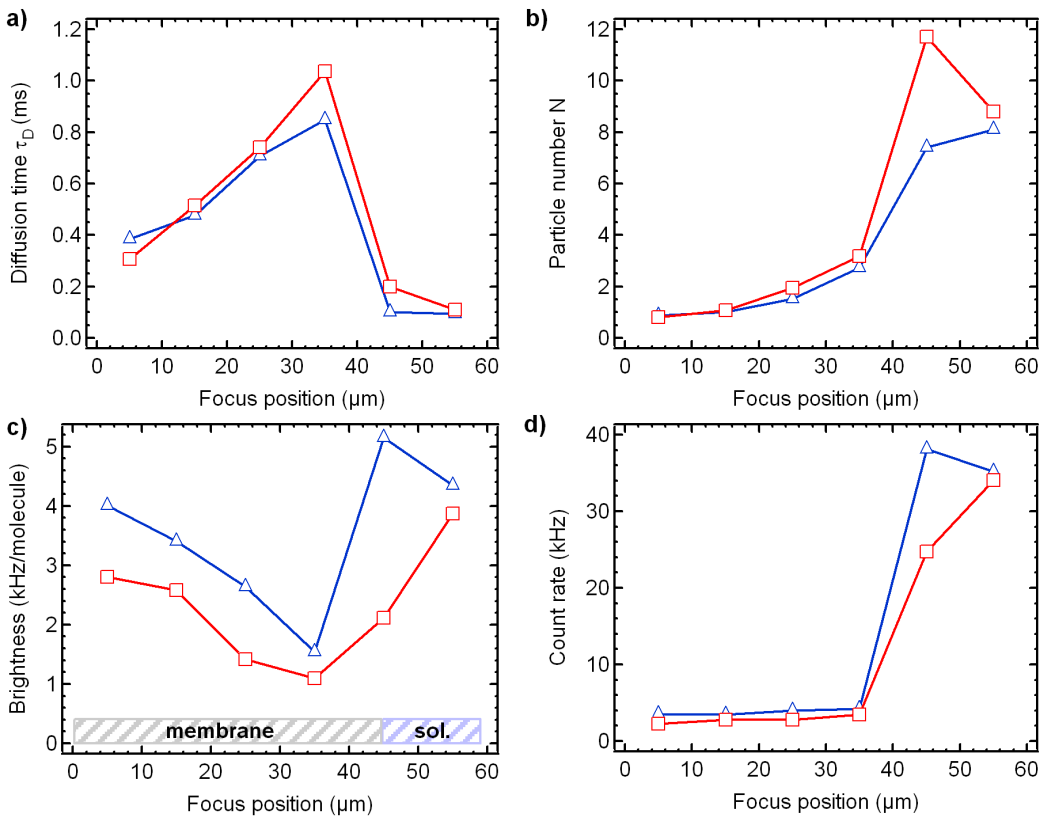

Figure 4.13: Alexa Fluor 488 diffusing within porous alumina (closed bottom) and in solution using an oil immersion objective. The measurements were performed using two excitation polarizations: 0° for the blue markers (-△-) and 90° for the red markers (-□-). All graphs are plotted as a function of the focus position, whereas the oil/membrane interface was set to zero: **a)** diffusion time τ_D, **b)** mean particle number N, **c)** molecular brightness B, and **d)** count rate.

maximum given by the numerical aperture of the objective. As shown in figure 4.13 **c)**, the molecular brightness is at this point almost as high as in free solution. From a more practical point of view, the usage of immersion oil to couple the membrane to the cover slide is very effective in terms of stability and reproducibiltiy.

Comparison of the objective configurations

As outlined in section 3.2, three different configurations were used for probing the diffusion in porous alumina. In each case, the membrane was glued onto a small glass tube. Whereas in the first two configurations the glass tube was pushed to the cover slide and the space between the membrane and the cover slide was either filled by water or immersion oil, the third configuration uses a linear actuator to position the glass tube in a larger, solution-filled chamber. The last configuration, which was mainly used in section 4.1, does not allow for scanning along the pores as the first two configurations do. However, using the third configuration enables the straightforward comparison of measurements in solution with measurements within the membrane because the measurement can be performed in the space between the coverglass and the membrane thus avoiding optical aberrations due to the membrane.
The drawback of this configuration is that, beside the impossibilty of accurate scanning, using a water-immersion objective for excitation and detection reduces the detection angle within the

membrane significantly. As discussed in section 4.1, almost half of the emitted intensity is lost for detection. The same problem occurs for the configuration with the pushed glass tube using the water-immersion objective, even if scanning along the pores is now possible.
The oil-immersion objective matches the refractive index of the water-filled alumina membrane quite well, even if the focus size along the optical axis is reduced in comparison to the water-immersion objective. It should be mentioned that by further tuning the porosity of the membrane, the effective refractive index of the membrane can be adjusted to the refractive index of glass. This would be the best choice for experiments where the knowledge about the size of the focus is mandatory.

4.3 1D-diffusion of eGFP: Changing *pH*-value

As discussed in section 4.1, the porous alumina membranes were incubated in bovine serum albumine (BSA) in order to prevent unspecific adsorption of the probes at the pore walls. However, it was shown that there is still a significant fraction of immobilized eGFP present within the membrane. This section deals with the diffusive behavior of eGFP within the membranes as a function of different *pH*-values without incubating the membranes in BSA beforehand. Therefore, the following set-up settings were used: the laser power of the diode laser operating at 488 nm was adjusted to 60 µW. The excitation was performed using linear polarized laser light. Behind the dichroic mirror, the remaining laser light was filtered using a 532 ± 35 nm bandpass filter. A 50/50 beam splitter was used to seperate the emitted light into two detectors for cross-correlation analysis. The membrane was fixed using the scheme shown in figure 3.2 **b)**. Excitation and detection was performed using the water-immersion objective. The drastic effect of changing the *pH*-value of the buffer solution is demonstrated in figure 4.14. Figure 4.14 **a)** shows the background intensity of the membrane, of the citrate buffer solution (10 mM citric acid and 100 mM potassium phosphate) and pure water for optical coupling of the membrane to the microscope cover slide. Figure 4.14 **b)** was recorded directly after addition of eGFP in order to obtain a concentration of 9.2 nM in solution. The green arrow indicates the consecutive scanning times. The penetration of the protein into the membrane starts slowly and can be tracked by the scanning image. After recording of 4.14 **b)**, the focus of the microscope was placed within the membrane, indicated by the green ellipse in figure 4.14 **c)**, and a stationary intensity time trace was recorded. Figure 4.14 **c)** shows the image recorded after finishing the transient time trace. No adsorbtion at the membrane/buffer interface and no bleaching in the region of the recorded time trace is visible. This indicates that a large fraction of the proteins is mobile. A different behavior can be found, if instead of *pH* 8 for the initial buffer a *pH*-value of 6 was used. Figure 4.14 **d)** was recorded after the addition of eGFP to the buffer, and after recording an intensity time trace at the position marked by the green ellipse. The first distinctive feature is the strong adsorption at the membrane/solution interface. Whereas the legend of the figure has a color range from zero to 120 photons/pixel, the count rate exceeded 5000 photons per pixel at the interface. Moreover, strong bleaching occured, which is an additional hint for a large fraction of immobilized molecules. According to the literature, the isoelectric point (IEP) of alumina is around $pH \sim 8-9$ [27, 108] and for (e)GFP around $pH \sim 5.5$ *[70]*. It was reported by Lau and coworkers that BSA shows the strongest adsorption behavior within alumina mem-

brane at its IEP of *pH*∼ 5 [57], regardless of the charge state of the adsorption surface [27]. Therefore, both the strong adsorption of eGFP at a *pH*-value of 6 and the lower adsorption behavior at higher *pH*-values can be explained, by assuming that both proteins with almost equal IEPs (eGFP and BSA) show a comparable adsorption behavior. Moreover, by testing different *pH*-values it was found that only at *pH*-values between *pH* 8 nad *pH* 11 bursts in the corresponding stationary intensity time traces were detectable within the membrane, whereas for lower *pH*-values the strong adsorption starting at the membrane/solution interface inhibited the detection of a diffusing fraction.

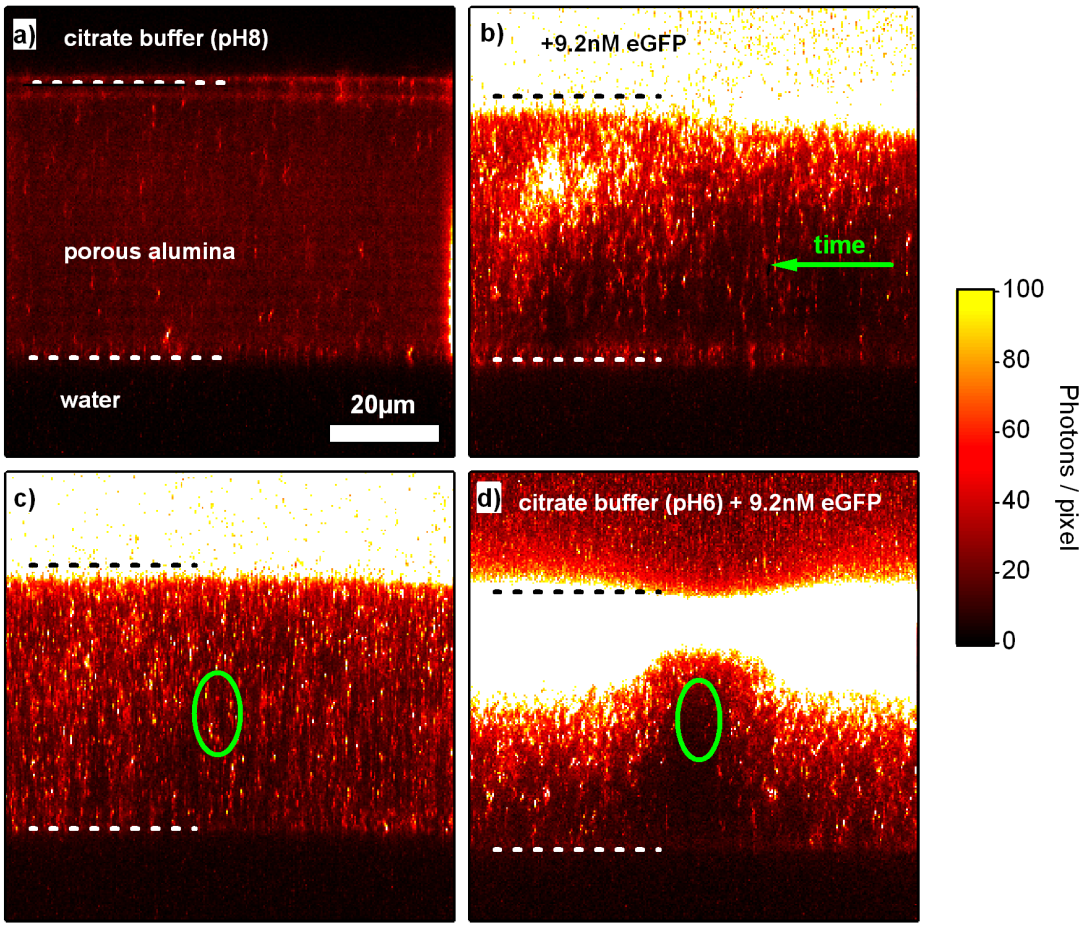

Figure 4.14: Color-coded scanning image of a buffer-filled porous alumina membrane. The membrane was attached via pure water to the cover glass using an water-immersion objective for excitation and detection. The size of the image is 60 µm x 60 µm scanned with a resolution of 256 x 256 pixels, recorded with a speed of 1 pixel/ms. The dashed lines represent the buffer/membrane and the pure water/membrane interface. **a)** Background intensity of a buffer-filled (*pH* 8) porous alumina membrane. **b)** Image recorded after adding several µl of eGFP in order to reach a concentration of 9.2 nM in solution. The green arrow indicates the direction, in which the focal volume was shifted during the series of consecutive measurements. The penetration of the dye into the membrane starts slowly. No adsorption is visible at the solution/membrane interface. **c)** Image recorded after taking a intensity time trace for several minutes at the position of the green ellipse: no bleaching visible. **d)** Instead of using a buffer with a *pH*-value of 8, a *pH*-value of 6 was used. The image was taken after recording an intensity time trace at the position of the green ellipse: strong bleaching is visible. In addition, a strong adsorption occurred at the solution/membrane interface where the count rate exceeded 5000 photons per pixel.

4.4 Monte-Carlo simulations of 1D and 3D diffusion

1D diffusion in single nanopores

As it has been shown in section 4.1, confined diffusion of single fluorescent molecules in nanoporous alumina can be explained with the model of quasi one-dimensional diffusion. Nevertheless, the complexity of the investigated system is still high. The auto-correlation curves, which fully represent the diffusional properties of the molecules in the system can be influenced by several effects: 1) the porous structure itself can contribute a background intensity signal, which leads to an increased apparent number of particles in the detection focus, 2) particles can interact with the porous structure. For example, particles can adsorb at the pore walls, which may lead to an uncorrelated background intensity, 3) the excitation/detection focus can be changed within the membranes due to the different refractive indices of the water filled porous structure and the used microscope objective, and 4) the auto-correlation fitting functions were derived for the case of infinite diffusional space. This is not fulfilled for the diffusion within a finite pore.

The simulations in the following section do not aim in covering the whole complexity of quasi one-dimensional diffusion in nanopores. In fact, the idea is to start with a simple model system. For the simplest case, the diffusion of single molecules was simulated in a single pore using a fully Gaussian excitation/detection focus. The diffusion coefficient was set to $D = 2.8 \cdot 10^{-6}\mathrm{cm}^2/\mathrm{s}$, which equals the diffusion coefficient of Alexa Fluor 488. The pore diameter was set to 30 nm and the size of the focus, which was placed in the center of mass of the pore, was defined by $w_0 = 250\,\mathrm{nm}$ and $z_0 = 1000\,\mathrm{nm}$ in agreement with the experiment. The excitation probability for a molecule in the center of the focus was set to $\rho = 0.2/\mu\mathrm{s}$. Figure 4.15 **a)** shows the normalized auto-correlation functions as a function of the pore length, which ranged from 5 µm to 60 µm (in steps of 5 µm), for the first boundary condition and **b)** for the second boundary condition. For the description of the boundary conditions see section 3.4. In the simulations using the first boundary condition, where movements which would cause the molecule to leave the pore are discarded, the shape of the auto-correlation changed dramatically for small pore lengths of less than 30 µm. Even for a pore length of 60 µm, the one-dimensional model (represented by the solid black line) according to equation 2.19 does not fit properly for times around 0.1 s. As it has been discussed above, the fitting functions were derived for the case that the molecules have an infinite space for diffusion. In conclusion, even if the pore length is much larger than the elongation of the focus in the z- direction, the calculated auto-correlation function is sensitive to the first boundary condition. The simulations, which are using the second boundary condition, show a completely different behavior. Here, each molecule which would leave the pore at the top side is virtually destroyed. However, at each time step there is a certain probability that a new molecule enters the pore. Only the auto-correlation function of the smallest pore featuring a length of 5 µm differs clearly from the other auto-correlation functions. For the case of pore lengths larger than 30 µm the fitting function matches almost perfectly the one-dimensional model.

Figure 4.16 **a)** shows the diffusion time τ_D as a function of the pore length for all boundary conditions as introduced in section 3.4. The dashed line represents the expected diffusion time which is calculated according to $\tau_{0,D} = z_0^2/4D = 0.89\,\mathrm{ms}$. Whereas τ_D is almost constant for

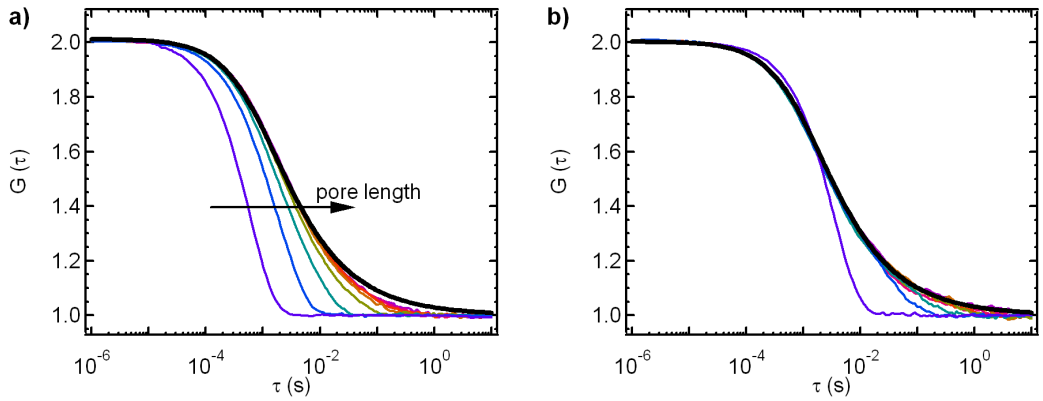

Figure 4.15: Simulated normalized auto-correlation functions of molecules diffusing in single pores with different pore lengths. The pore lengths range from 5 µm to 60 µm. The simulations in **a)** are using the first boundary condition: movements, which would cause the molecules to leave the pore are discarded, the simulations in **b)** are using the second boundary condition: molecules, which leave the pore at the top are destroyed. Nevertheless, new molecules can enter the pore with a certain probability. The black lines show the corresponding fits for pores with a length of 60 µm.

the second boundary condition above a pore length of 5 µm, the first and the third boundary condition leads to a different behavior. Here, τ_D increases without reaching the expected value even for a pore length of 60 µm. This finding can be explained by the fact that the boundary conditions that prevent the molecules from vanishing, impose some periodicity to the diffusional system. Each molecule will re-enter the focus within a certain timeframe if it is reflected by the lids of the cylinder (pore). This periodicity is broken if the molecules can diffuse away from the pore, as it is possible only in the case of the second boundary condition.

The question remains why the calculated τ_D value using the second boundary condition is larger than the expected value $\tau_{0,D} = 0.89$ ms in most cases. To answer this question, we have to consider the other graphs in figure 4.16. Figure 4.16 **b)** shows the mean particle number N as a function of the pore length. Except for a pore length of 2.5 µm, the initial concentration for each pore length was one particle per 5 µm pore length. The smallest pore initially contained one particle, and thereby twice as much particles per length. However, even under this assumption the calculated mean particle number is too high for the first and the third boundary condition which can be explained by the fact that the pore length is even smaller than the long axis of the detection focus. If the pore length is 10 µm or larger, N remains constant.

Simulations using the second boundary condition show a different behavior. Here, N is smaller as compared with the other boundary conditions and is increasing with increasing pore length. This effect is caused by the possibility of changing the concentration within the pore when molecules either can leave the pore or enter the pore. If the rate at which molecules leave the pore is initially larger than the rate at which particles enter the pore, the mean particle number decreases until a new equilibrium is reached. The auto-correlation function is averaging the mean particle number over the whole duration of the simulation. Thus, the decrease in the particle concentration in a small pore is faster than in a large pore and leads to smaller mean particle numbers as seen in the graph. This decrease in concentration does additionally affect the auto-correlation function, which normally decays to unity for infinite times, in such a way that an offset in $G(\tau)$ is induced. The (small) offset cannot be fitted using the normal one-

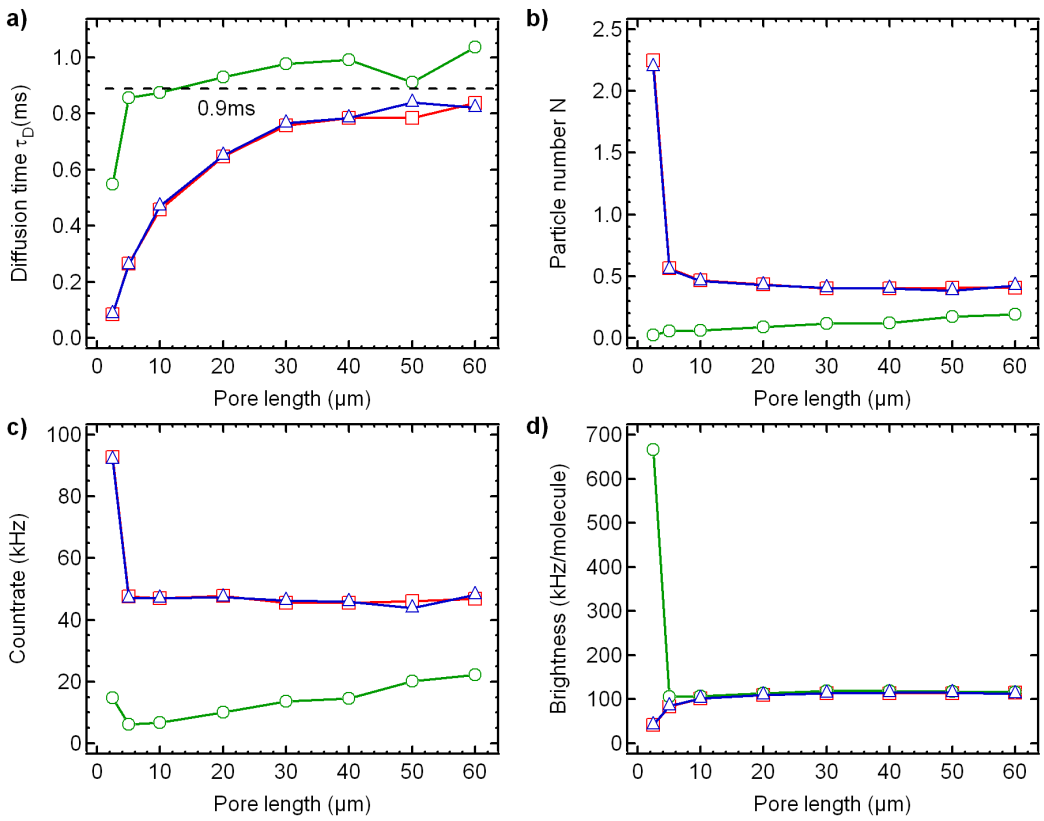

Figure 4.16: Various simulated parameters describing the diffusion properties as functions of the applied boundary condition and the length of the pore. Three different boundary conditions have been used: (-□-) as the first, (-◯-) as the second and (-△-) as the third boundary condition as discussed in section 3.4. The diffusion time τ_D as a function of the pore length is shown in **a)** Here, the expected diffusion time $\tau_D = 0.9$ ms is represented by the dashed line. The brightness B as shown in **b)** is calculated from the mean count rate shown in **d)** divided by the mean particle number N as shown in **c)**.

dimensional fitting function and will lead to a change in the determined diffusion time τ_D as it can be seen for the diffusion time calculated from the simulations with the second boundary condition. Figure 4.16 **c)** shows the mean count rate as a function of the pore length. For the first and third boundary condition, the count rate reproduces perfectly the molecule concentrations, which are constant with the exception of the doubled molecule concentration in the smallest pore. The second boundary condition shows an interesting feature for the smallest pore, where the count rate is higher than for the longer pores. Again, this can be explained by the given probability that a new molecule can enter the pore. In most cases, this molecule will disappear very soon. However, molecule is generated close to the focus, there will be a certain probability that the molecule is excited and emits photons without significantly contributing to the auto-correlation function. The evaluation of the brightness in figure 4.16 **d)** supports this finding: if the calculated mean number of molecules is small but the count rate is high, the molecule shows a very high apparent brightness. If the pores are larger than 5 µm, the brightness $B \simeq 100$ kHz is equal for each of the boundary conditions.

Another problem to be addressed is whether the position of the excitation/detection focus with respect to the pore does play a role for the obtained auto-correlation function. Figure 4.17 **a+b)** shows the diffusion time τ_D and the mean particle number N as a function of the position of

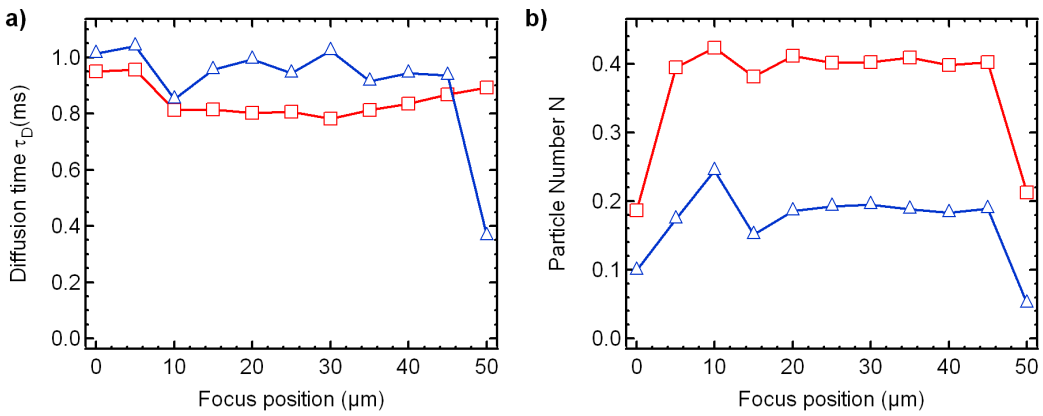

Figure 4.17: a+b) Simulated diffusion time τ_D and mean particle number N as a function of the position of the focus in a single pore with a length of 50 µm. Two boundary conditions were used: (-□-) as the first and (-△-) as the second boundary condition, as discussed in section 3.4.

the focus within a single pore with a length of 50 µm. The focus position of 0 µm corresponds in all cases to the closed side of the pore, where possible movements out of the pore are discarded according to the first boundary condition. Due to impedement of motion out of the pore, the mean diffusion time is slightly extended at this point. It has to be mentioned that half of the focus is out of the region of interest, which has almost no influence on the diffusion time, however, the mean particle number drops by a factor of two. The decay of the auto-correlation curve is only given by fluctuations in the intensity and not by the (mean) intensity itself. Nevertheless, the auto-correlation function is normalized by the squared (mean) intensity. For this reason, it is obvious that in the case of the diffusion time the pore bottom acts like a mirror of the fluctuations, whereas for a constant concentration of molecules within the pore the count rate is expected to decrease by a factor of two, thus perfectly matching the decrease of the mean particle number N.

At the focus position of 50 µm an additional effect occurs for the case of the second boundary condition. The diffusion time is drastically smaller because the molecule can disappear through the opening of the pore. Even if there is a certain probability that a new molecule enters the pore at the top, in most cases the new molecule will rapidly diffuse away.

In conclusion, the simulations confirm the quasi-one dimensional diffusion model quite well as long as the pore length is larger than 30 µm and the pore diameter is small in comparison with the dimensions of the focus in the x- and y-plane. Additionally, it was found that the boundary conditions play an important role in the interpretation of the obtained results.

1D diffusion in pore arrays and 3D diffusion

We will now extend the simulations by taking into account that in the experiment more than one pore is located within the focus. As discussed in section 4.4, this can be realized by creating a virtual hexagonally ordered pore array. Every molecule is randomly placed in one of the 60 pores. The generated hexagonal pore array consists of a central pore and the pores within an area with a radius corresponding to the eight-nearest neighbor distance. If the lattice constant is set to 65 nm, this distance is 260 nm, which corresponds to the small half axes $w_0 = 250$ nm of the excitation/detection focus. Larger pore arrays can be taken into account, nevertheless,

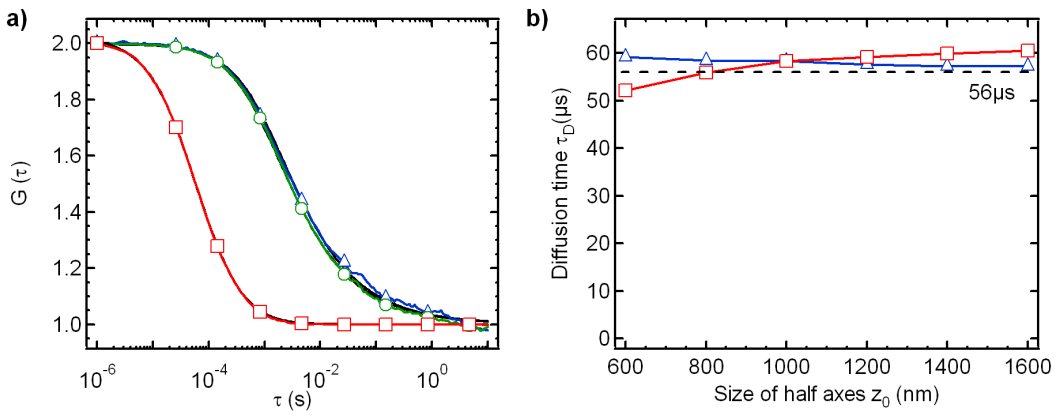

Figure 4.18: **a)** Comparison of the simulated normalized auto-correlation functions between three-dimensional diffusion (-□-), in this graph, the symbols represent every 20th data point), one dimensional diffusion in a single pore (-◯-) and one dimensional diffusion in an array of pores (-△-). For the simulations of one-dimensional diffusion the second boundary condition was used. The solid black lines (almost invisible behind the calculated auto-correlation lines) show the corresponding fits. **b)** Influence of the focus size in the z- direction (represented by z_0) by using a fixed w_0 on the diffusion time for the case of three-dimensional diffusion. The ratio of z_0/w_0 represents the structure factor s of the focus. If the structure factor is set to $s = 4$ for all auto-correlation functions, the boxed values (-□-) are calculated. If the structure factor is set to z_0/w_0 according to the initial parameters for the simulations, the triangled values (-△-) are calculated. Here, the expected diffusion time of $\tau_D = 56\,\mu s$ is shown by the dashed line.

the computation time increases rapidly if the concentration of molecules within the pores is kept constant and thereby the number of simulated molecules has to be increased. Figure 4.18 **a)** shows the calculated auto-correlation function for the simulation of the three-dimensional diffusion, the quasi one-dimensional diffusion in a single pore and the quasi one-dimensional diffusion in an array of pores. The auto-correlation function of three-dimensional diffusion decays much faster than for the one-dimensional case, because a molecule can diffuse out of the focus volume in any direction. Moreover, the auto-correlation functions of the two cases of one-dimensional diffusion almost coincide. Only at timescales in the millisecond range slight deviations occur, which can be attributed to the different brightness of both variants. For the case of diffusion along the single pore, where the origin of the excitation/detection focus is in the center of mass of the pore, the expected photon count rate is higher than for a molecule diffusing in a pore, which is almost at the edge of the focus. Keeping in mind that the shape of focus is similar to a rotational ellipsoid, the brightness calculated for one-dimensional diffusion in a pore array is about 50% of the brightness in a single pore ($B_{1D}^{Array} = 65\,kHz/molecule$, $B_{1D}^{sPore} = 121\,kHz/molecule$). The brightness for the three-dimensional case $B_{3D} = 59\,kHz/molecule$ is even slightly lower, because the number of pores in the pore array is still too small to recover all contributions of the whole focus.

I will now concentrate on the diffusion time for the case of three-dimensional diffusion. As shown in figure 4.18 **a)**, the corresponding fitting function for the auto-correlation function matches perfectly the simulations. For simulating the three-dimensional diffusion inside a cylinder, the height of the cylinder was set to 5 µm and the diameter was set to 3 µm. Figure 4.18 **b)** shows the diffusion time as a function of z_0, which is the size where the maximum intensity of the Gaussian focus drops to $1/e^2$ along the z-axis. Changing z_0 by fixing $w_0 = 250\,nm$ will

change the structure factor $s = z_0/w_0$. If the fitting functions for the two-dimensional case of diffusion (equation 2.20) are compared with the three-dimensional one, (equation 2.21), they only differ in a single term. If $z_0^2 \gg w_0^2$, this additional term contributes only slightly to the fitting procedure. For this reason, the diffusion time τ_D is almost insensitive to the size of the half axes z_0. Even if the fitting is performed with a fixed structural parameter of $s = 4$ for all cases, the deviation from the expected theoretical value of $\tau_D = w_0^2/4D = 56\,\mu s$ as represented by the dashed line is negligible. In conclusion, whereas for the case of three-dimensional diffusion the diffusion time is mainly sensitive to the size of the focus in the x-, y-plane, in the case of one-dimensional diffusion along the pores the diffusion time $\tau_D = z_0^2/4D$ is highly sensitive to z_0 .

Monte-Carlo simulations of spFRET in solution

This subsection deals with the simulation of doubly labeled proteins diffusing either in solution or in an array of pores. These doubly labeled proteins can untergo conformational changes. Thus, the distance between the attached dyes (labels) changes, which results in different energy transfer rates from the donor to the acceptor dye. Calculating this energy transfer efficiency has been a major challenge in recent years [104, 89, 72]. Two different approaches can be used to determine the transfer efficiency E by using the detected transient time traces. For the first one, each bin is used for calculating E according to equation 2.12, as long as the sum of both intensites per bin is above a certain threshold. Normally, a binwidth of 500 µs is used for binning the transient time traces. This value has to ensure that, on the one hand, a molecule diffusing through the focus emits enough photons in this time to be statistically relevant and, on the other hand, that the counting of background intensity is minimized. Additionally, it has to be ensured that no averaging over different molecules takes place. The second approach of determing the transfer efficiency is slightly different. Here, a burst is defined and integrated intensities within each burst are used to calculate E [72, 17]. For the sake of simplicity, the proposed burst-search algorithm was modified in the following way, still making use of the binned transient time traces. Photons belong to a burst if at least $L = 50$ phontons are detected in a number of consecutive bins with at least $M = 30$ photons per bin. Figure 4.19 **a+b)** shows snapshots of the transient time traces of the donor and the acceptor channel for doubly labeled proteins diffusing in bulk solution (**a**) and within an array of pores (**b**), respectively. In addition, the burst-search algorithm was applied to the sum of both time traces of each graph. This algorithm gives "1" if the bin corresponds to a burst otherwise "0". As seen in figure 4.19 **a+b)** the transients differ in their shape with respect to the dimensionality of diffusion. Whereas in 4.19 **a)** the width of the burst is given by one bin only, the width of the bursts in 4.19 **b)** is mostly larger. To give a more qualitative picture, the number of bursts as a function of the number of bins per burst is plotted in 4.19 **c)**. Comparing the three-dimensional case of diffusion with the one-dimensional case, two distinctive features should be noted. First, the overall number of bursts and second, the average number of bins per burst is much smaller in the case of the three-dimensional diffusion. This results in an increased number of photons per bin as compared to the one-dimensional diffusion as seen in figure 4.19 **d)**. The simulated time was equal for both cases of diffusion. In addition, a certain probability of $\rho_{T,D} = 0.1$ for

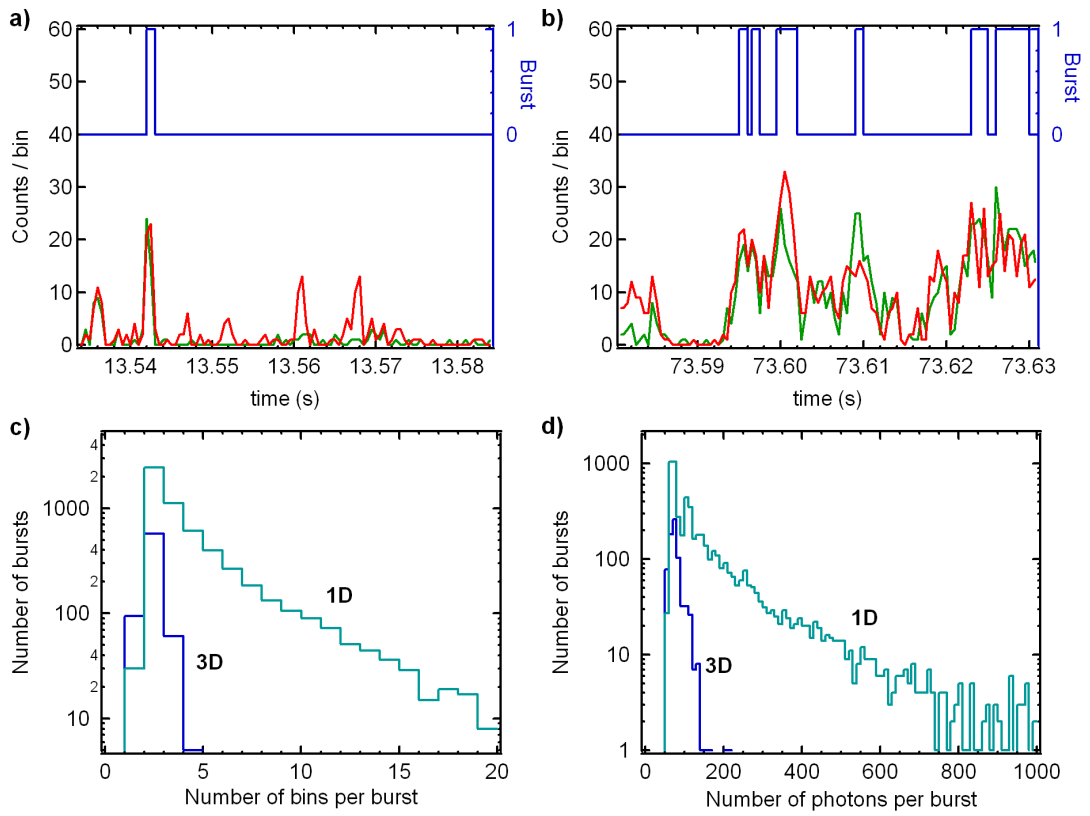

Figure 4.19: Simulation of doubly labeled proteins diffusing either in free solution or in an array of pores. **a+b)** Transient time traces of the protein: the green line represents the detected intensity in the donor channel and the red line in the acceptor channel, respectively. Both intensities are summed up for each bin, and a burst-criterion (see text for details) is applied. The burst trace (blue line) is either "1" if a bin belongs to a burst otherwise "0". **a)** Simulations of diffusion in free solution and **b)** in an array of pores. **c)** Number of bursts as a function of the number of bins per burst. **d)** Number of bursts as a function of the number of photons per burst.

the donor and $\rho_{T,A} = 0.2$ for the acceptor was included for relaxation of excited states to non-fluorescent triplet states with a time constant of $\tau_T = 10\,\mu s$. In order to check the mean particle number N within the excitation/detection focus, the auto-correlation functions were calculated for both time traces detected in the donor channel. Figure 4.20 shows the auto-correlation function for the cases of quasi one-dimensional and three-dimensional diffusion. Again, the diffusion time is increased in the case of quasi one-dimensional diffusion. This increased diffusion time is highly advantageous for the separation of different compartments of the auto-correlation function. Whereas in the one-dimensional case the two contributions to intensity fluctuations, namely diffusion and triplet dynamic, can be clearly separated, the excistence of two components instead of one in the case of three-dimensional diffusion is easily overlooked. Here, the confined diffusion is a suitable tool to study dynamics of single molecules on time scales which are normally dominated by diffusion.

The mean particle numbers calculated by using appropriate fitting-functions are almost equal. As discussed above, the quasi one-dimensional diffusion shows a pronounced burst-like behaviour. The question arises whether this feature is useful for the determination of energy transfer efficiencies. In addition to the different cases of diffusion, the two possibilities of calculating the transfer efficiencies, namely the bin- and the burst-approach, are elaborated in

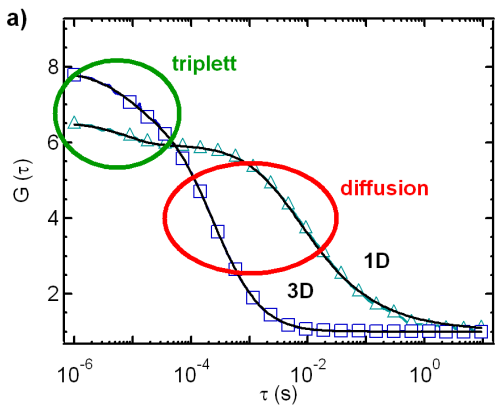

Figure 4.20: Simulated auto-correlation functions of the donor channel showing the differences in diffusion time for three-dimensional diffusion (-□-, symbols represent every 10th data point) and quasi one-dimensional diffusion (-△-), respectively. Here, a triplet-fraction was included in the simulations. This fraction is only clearly separable from the time-domain of diffusion in the case of 1D-diffusion. The solid black lines show the corresponding fits.

detail. The simulations were performed using equal time-constants for the folded ⇌ unfolded

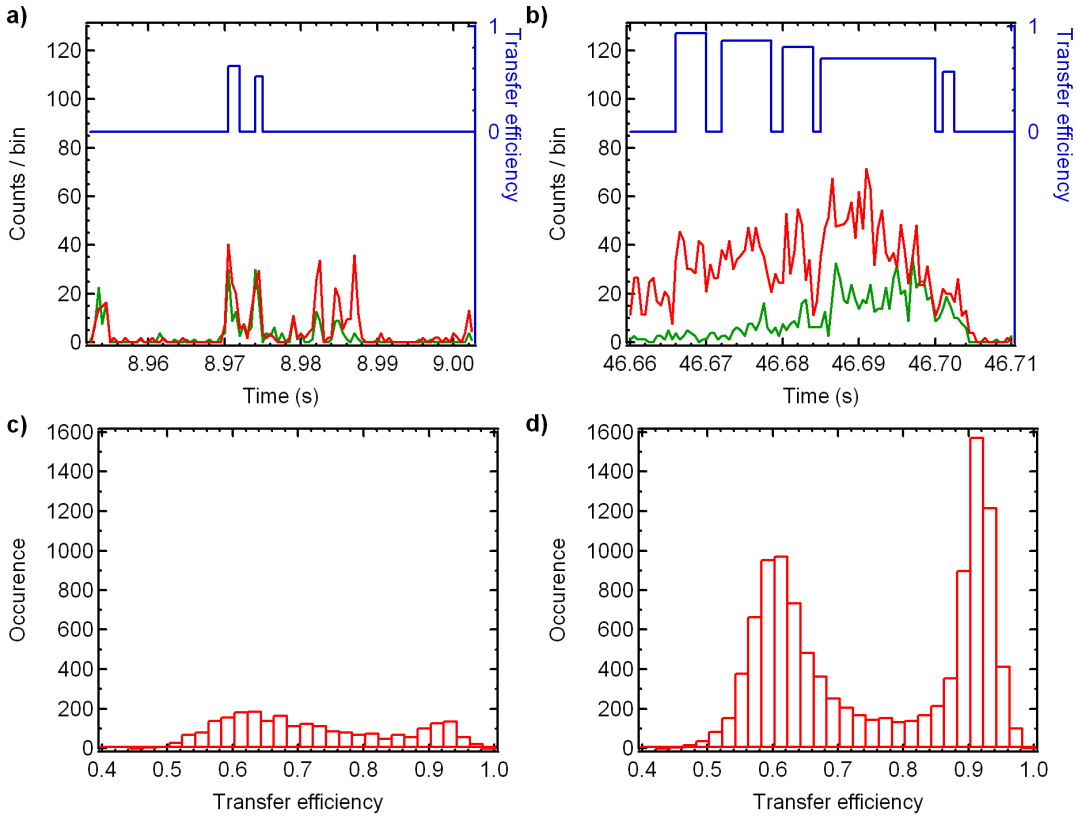

Figure 4.21: Simulation of doubly labeled proteins diffusing either in free solution or in an array of pores. **a+b)** Quantum yield-corrected transient time traces of the protein: the green line represents the detected intensity in the donor channel and the red line in the acceptor channel, respectively. Both intensities are summed up for each bin, and a burst-criterion (see text for details) is applied. The transfer efficiency was calculated according to equation 2.12 for each burst. **a)** Simulations of diffusion in free solution and **b)** in an array of pores. Histograms of the transfer efficiency **c)** in free solution and **d)** in an array of pores.

transitions. The quantum yield for the donor was set to $\Phi_{f,D} = 0.8$ and for the acceptor to $\Phi_{f,A} = 0.5$. These values are neccesary for calculating the transfer efficiency using equation 2.12. Ideally, both quantum yields are close to unity. Unfortunately, this condition is never fulfilled under experimental conditions. According to chapter 3.4, the detection efficiencies of both channels were set to one. Figure 4.21 **a+b)** shows the quantum yield corrected transient donor and acceptor time traces for 1D and 3D diffusion. In addition, the transfer efficiency is shown for each burst. Here, the burst-search criterion was slightly modified to match the conditions for the corrected time traces. The minimum number of photons per bin was reduced to $M = 20$, and the minimum number of photons per burst was increased to $L = 100$. The histograms of the transfer efficiencies per burst are plotted in figure 4.21 **c+d)**. Both figures show two distributions corresponding to the folded and the unfolded states of the diffusing proteins. Nevertheless, the histograms for 1D diffusion contain a larger number of bursts, and even more important, the relative width of the distributions is smaller than in the 3D case of diffusion.
In conclusion, calculating the transfer efficiencies by applying the burst-search algorithm benefits massivly from the prolonged diffusion time in the case of one-dimensional diffusion. The key point is the increased number of detectable photons per burst, which decreases the relative width of the distributions. This is of considerable importance if a larger number of sub-populations is studied (for example with two doubly-labeled species), where the ability to distinguish these populations in the transfer efficiency histogram is mandatory.

4.5 FRET in porous alumina

This section presents first results of the detection of FRET in nanoporous alumina membranes. Barstar 488/594 was introduced in section 3.3 as a small protein, which was additionally labeled with a donor dye (Alexa Fluor 488) and an acceptor dye (Alexa Fluor 594) [45]. The set-up was modified in order to fulfill the requirements for the detection of the energy transfer. The excitation laser power of the 488 nm continuous-wave diode laser was set to 80 µW. A 570 nm dichroic beamsplitter was used to separate the light emitted from the donor and the acceptor into the corresponding green and red detector channel. Furthermore, the light was filtered using a 532±35 nm bandpass filter for the green channel and a 650±50 nm bandpass filter for the red channel. An oil-immersion objective was used for detection. The membrane was attached to the cover slide using a thin (10 µm) layer of immersion oil and the membrane was fixed with respect to the scanning device. The scanning along the membrane was performed by using a 80 x 80 µm scanning area, rastered with a local resolution of 256 x 256 pixels and a time resolution of 1 ms/pixel. Figure 4.22 **a+b)** shows the background intensity in the green and the red detection channel, respectively. Comparing the intensities in the green and the red detection channel reveals that the background intensity of the buffer is slightly lower and the background from the membrane is slightly higher in the red detection channel. The detection efficiency of the photodiodes increases at higher wavelengths. Nevertheless, the background intensity is relatively low, and can be further decreased by bleaching with the laser at a fixed position within the membrane. Figure 4.22 **c+d)** was recorded after addition of several µl of Barstar 488/594 solution in order to reach a concentration of 6.2 nM in solution. Figure 4.22 **c)** shows a strongly increased intensity in the buffer and the stripelike behavior of proteins

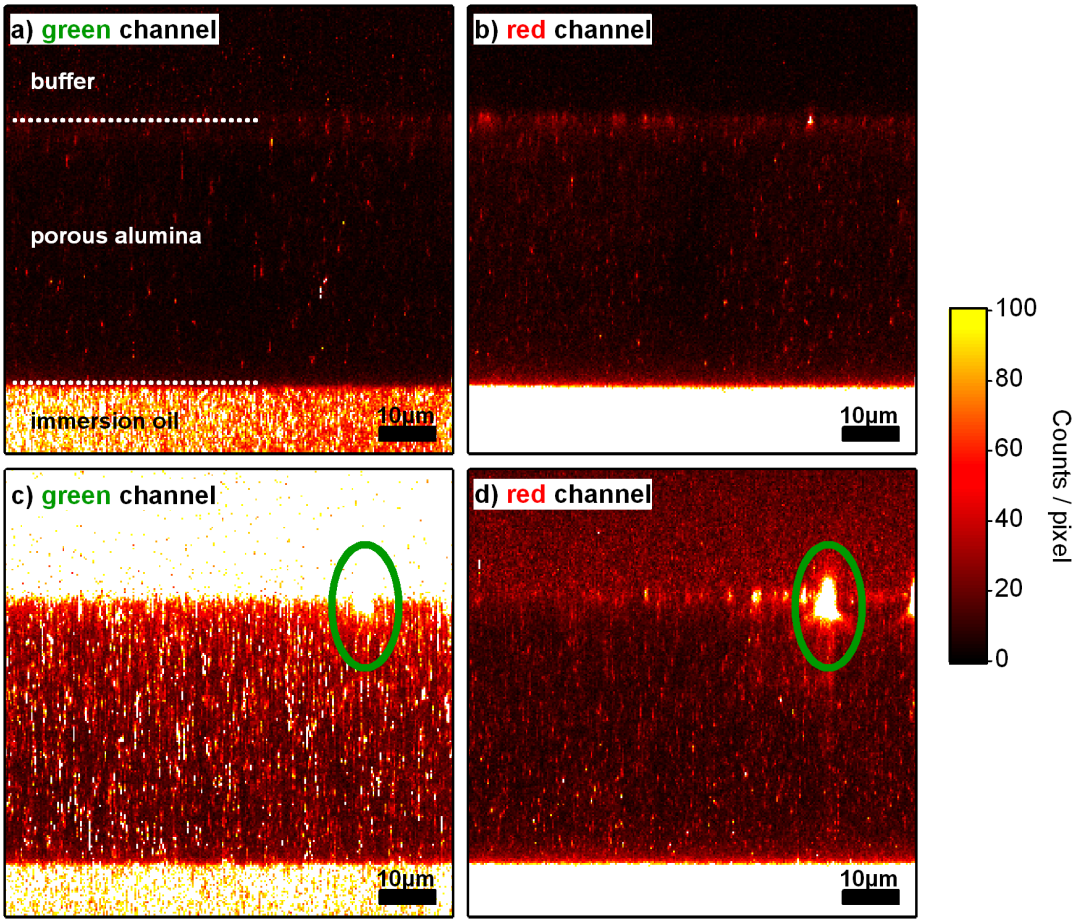

Figure 4.22: Color-coded scanning images of a citrate buffer-filled porous alumina membrane. The membrane was attached via immersion oil to the cover glass using an oil-immersion objective for excitation and detection. The size of the image is 80 µm x 80 µm scanned with a resolution of 256 x 256 pixels. The dashed lines represent the buffer/membrane and the membrane/oil interface. **a+b)** Background intensity of the buffer-filled membrane in the green channel and in the red channel. **c+d)** Scanned images of the green and the red channel after addition of 6.2 nM Barstar 488/594 solution. The green ellipse represents a defect in the membrane with strong adsorption of Barstar 488/594.

penetrating the membrane. However, the increase in the intensity in the red channel is only moderate. The reason for this is twofold: the quantum yield of the acceptor is significantly lower than the quantum yield of the donor ($\Phi_A = 0.22$ in contrast to $\Phi_D = 0.79$) and the labeling stoichiometry is disadvantageous. Two times more proteins are labelled only with a donor than being correctly labelled with a donor and an acceptor [45]. The area enclosed with the green ellipse can be either attributed to a defect in the membrane resulting in a stronger adsorption at this place or to an adsorbed aggregated protein complex. Nevertheless, raster-scanning of the membrane can be used to avoid taking measurements at these points. After directly placing the focus in the center of the images in figure 4.22, each time trace was recorded for 30 minutes in order to get sufficient statistics. Figure 4.23 **a)** shows a part of one recorded transient intensity time trace. Here, the intensities in the green and red channel were plotted as a function of time with a resolution of 500 µs per bin. It should be noted that the traces were directly corrected for the quantum yield of the fluorophores ($\Phi_A = 0.22$ and $\Phi_D = 0.79$) and the detection effciency in both channels ($\eta_A = 0.33$ and $\eta_D = 0.44$) [45]. A burst-like behavior

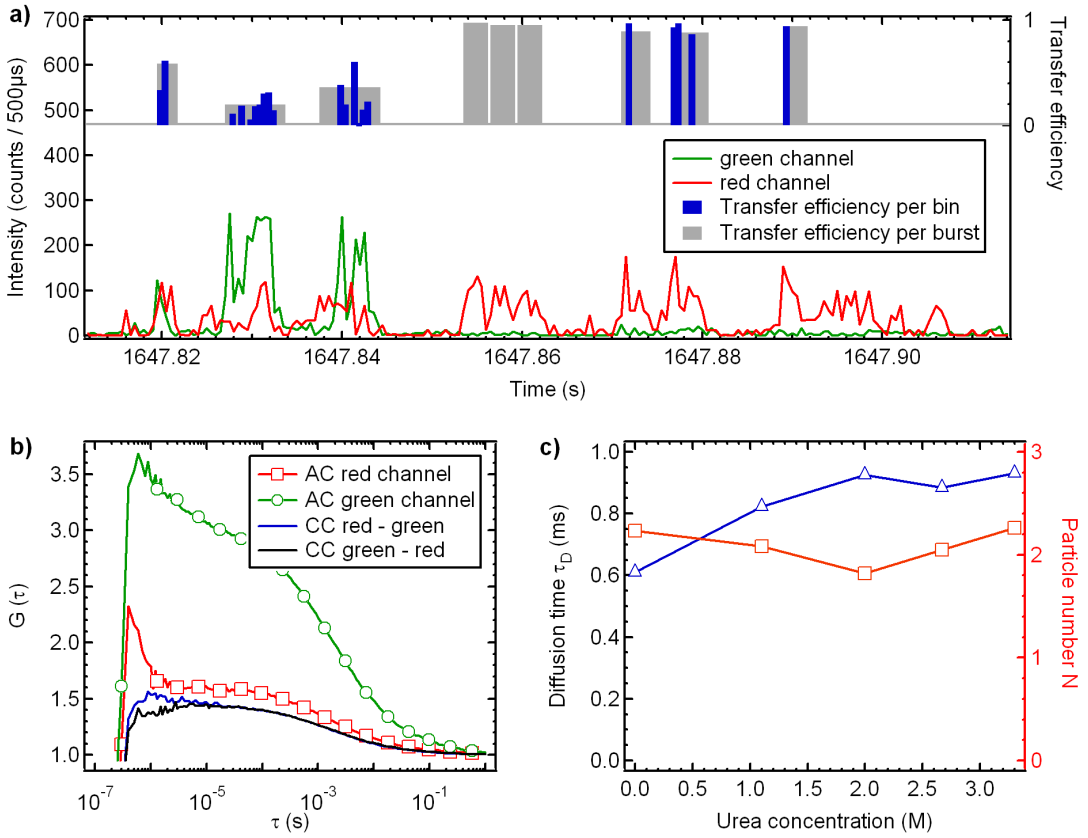

Figure 4.23: Analysis of measured time traces. **a)** (left axis) Cutout of the corrected timetraces in the green and the red detection channel as a function of time. (right axis) Calculated transfer efficiencies using a bin-based analysis (blue bars) and a burst-based analysis (gray bars). **b)** Auto- and cross-correlation functions for each possible constellation. **c)** Diffusion time τ_D and mean particle N as a function of the urea concentration.

was found, which can be analyzed in different ways. The simpliest method is to calculate the transfer efficiency for each single bin using equation 2.8 with $\gamma = 1$, because the correction was directly applied to the time traces. The blue bars in figure 4.23 **a)** correspond to the transfer efficiency per bin if the overall intensity of both channels exceeds 120 photons per bin. The gray bars in figure 4.23 **a)** correspond to bursts, which were found by the applied burst-search algorithm introduced in section 4.4. Due to the direct correction of the time traces, the criterion for the burst recognition was modified in the following way. Photons belong to a burst if at least $L = 300$ photons are detetcted in a number of bins with at least $M = 50$ photons per bin. The advantage of the burst-approach is that the history of an event can be used to obain a higher number of photons per burst than it is possible for a single bin. Thus, events can be used for calculating the transfer efficiency which would normally be discarded because they do not meet the threshold criterion of the single bin-approach. Moreover, detecting a higher photon number by averaging over several bins will give better statistics for the transfer efficiency histograms. Figure 4.23 **b)** shows the auto- and cross-correlation functions for each possible constellation. All correlations show the prolonged diffusion time of one-dimensional diffusion. Comparing the amplitudes of the auto-correlation functions in the green and the red channel, respectively, the amplitute is higher for the green channel, implying an apparent smaller particle number. However, as known from the stoichiometry of the protein labeling, more donor-only proteins

are expected than molecules bearing both donor and acceptor. This finding can be explained by the strong influence of the background intensity especially for the red channel. Measuring the transfer efficiencies is performed with very low concentrations of the probes. Thus, the influence of the background either from the membrane or adsorbed molecules can be huge. Both auto-correlation functions show an increase in the correlation at time scales around 1 µs, which can be attributed to afterpulsing, and around 10 µs, which can be attributed to populated triplet states.

In addition, figure 4.23 **b)** shows the two cross-correlation functions of the red versus the green channel and the green versus the red channel. The slight discrepancy of both functions at short time scales is an experimental artifact caused by the detection electronics. Nevertheless, calculating the cross-correlation functions allows varifying the strong relation between the appearance of bursts in the red and the green channel. For example, after measuring the diffusion of a red and a green dye, which are not linked by a protein backbone, no cross-correlation function would be observable in contrast from being one for all times. Therefore, the excistence of a cross-correlation functions is a clear evidence for donor/acceptor labeled molecules diffusing through the detection focus.

Barstar 488/594 is a small protein and can be unfolded using urea. By unfolding the protein, the mean distance between the fluorophores increases and a drop in the transfer efficiency should be detectable. Here, a 8 M urea solution was added stepwise to force the unfolding of the protein. Between each step, transient intensity time traces were recorded within the membrane. As shown in figure 4.23 **b)**, the diffusion time, which was calculated using the red versus green cross-correlation function, increased from around $\tau_D = 0.6$ ms to around $\tau_D = 0.9$ ms. The increase in the diffusion time can be attributed to several reasons: 1) the effective refractive index of the buffer- and urea-filled membrane changes due to the high concentrations of urea, which leads to a change in the size of the excitation/detection focus and 2) the (partial) unfolding of the protein leads to a different effective diffusion coefficient due to its increased hydrodynamic radius and its increased number of binding sites offered to the pore walls. However, the diffusion times are rather small for a protein. Similiar diffusion times were measured for freely diffusing dyes. Photobleaching due to the high excitation power is another effect, which might be responsible for the small diffusion times. If a fluorophore diffuses into the focus and bleaches, the auto-correlation function will interpret this result as an apparent shorter diffusion time.

The transfer efficiency histograms of Barstar 488/594 for different concentrations of urea are shown in figure 4.24. In general, three different regions can be defined for each histogram: 1) donor-only 2) donor + acceptor: unfolded conformational state, and 3) donor + aceptor: folded state. The first region (donor-only) shows low transfer efficiencies, as they are calculated for proteins, where only a donor is attached. Nevertheless, the correction for the low acceptor quantum yield introduces an artifical amplified background intensity in the red detection channel, which can not be prevented. Moreover, the uncorrelated background fluorescence of the membrane, which is in almost any case higher than in bulk solution, causes an additional broadening of the peak up to apparent transfer efficiencies of 0.5 - 0.6. Within the second region, the peak corresponds to the unfolded protein with a larger donor to acceptor distance than in the folded state, which belongs to the third region. It was shown by Hofmann and coworkers for

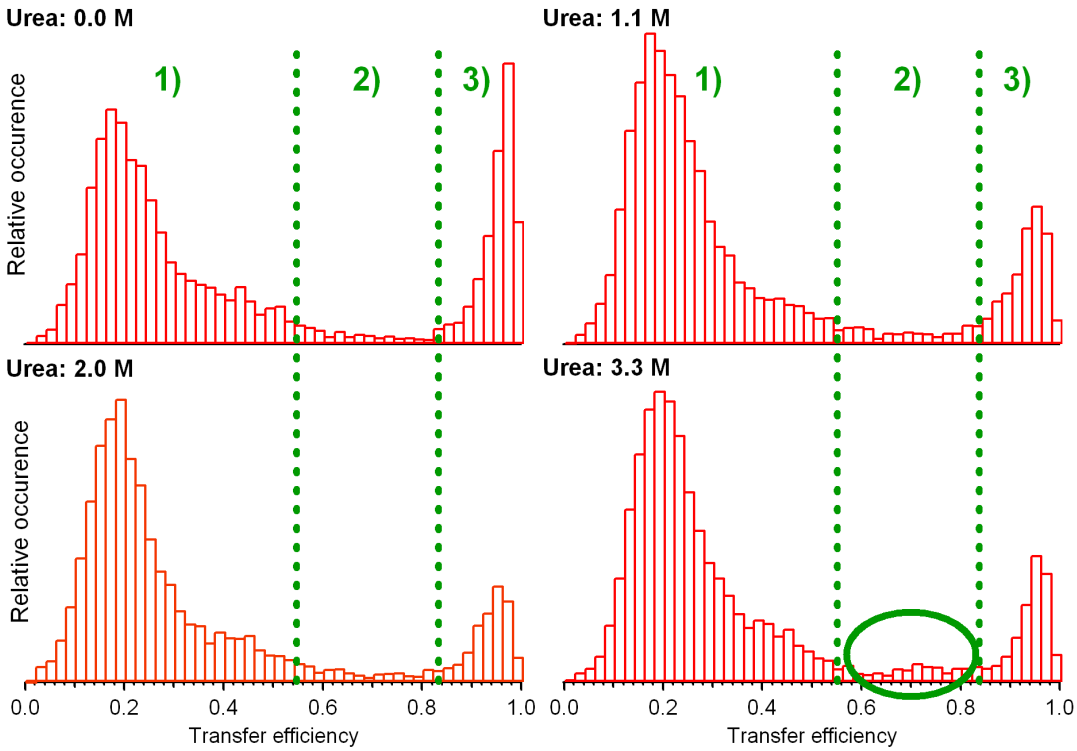

Figure 4.24: Histograms of the calculated transfer efficiencies for different concentrations of urea. For each concentration, the corrected transient timetraces were analayzed using a burst-search algorithm. The green ellipse indicates the area, where the peak of the unfolded protein was expected.

Barstar 488/594 diffusing in free solution that the peak position of the unfolded proteins shifts from around 0.7 for an urea concentration of 1.1 M to 0.55 for an urea concentration of 5.2 M [45]. The folding to unfolding transition is reversible for Barstar 488/594. The equilibrium of folded and unfolded proteins (equal rate constants for folding / unfolding) is attained for a urea concentration of around 2 M.

As shown in 4.24, the first and the third region are populated for each concentration of urea whitin the solution. However, no significant unfolded population occurs in the measurements. Only a very small peak can be seen for the highest urea concentration (marked by the green ellipse). These histograms differ from those obtained with free solution, where a significant fraction of unfolded proteins was found for urea concentrations higher than 1 M. There are a number of open questions which cannot be answered yet: 1) What is the actual concentration of urea within the pores? 2) Does the urea adsorb on the pore walls? 3) What is the influence of the single fluorophore on the diffusive behavior of the labeled protein within the membrane? 4) Are the rate constants of folding/unfolding within the membrane equal to those in free solution? As mentioned above, the experiment suffers from a number of drawbacks in particular the low acceptor quantum yield and the unsatisfying stoichiometry. Moreover, using an acceptor dye which can be directly excited by a pulsed laser would allow using more sophisticated energy transfer detection schemes as introduced in section 2.4. With such a scheme, the sorting of proteins in respect to their degree of labeling is possible and allows, for example, to discriminate between low-FRET proteins and proteins which are only labeled with a donor dye.